*Carbon Energy*

WILEY

CARBON ENERGY

RESEARCH ARTICLE OPEN ACCESS

# Alloying Cu, Fe, and Co in Ni/YSZ Electrodes for High-Temperature $CO_2$ Electrolysis: Impact on TPB Density, Activity, and Carbon Deposition Resistance

Min Jun Oh[1,2] | Sooin Lee[3] | Jeeho Hong[1,4] | Kyung Joong Yoon[1] | Ho-Il Ji[1,5] | Ji-Won Son[1,4] | Jong-Ho Lee[1,5] | Kyeounghak Kim[3] | Jongsup Hong[2] | Sungeun Yang[1,5]

[1]Center for Hydrogen Energy Materials, Korea Institute of Science and Technology (KIST), Seoul, Republic of Korea | [2]School of Mechanical Engineering, Yonsei University, Seoul, Republic of Korea | [3]Department of Chemical Engineering, Hanyang University, Seoul, Republic of Korea | [4]Graduate School of Energy and Environment (KU-KIST Green School), Korea University, Seoul, Republic of Korea | [5]Division of Nanoscience & Technology, Korea University of Science and Technology, KIST Campus, Seoul, Republic of Korea

**Correspondence:** Jongsup Hong (jongsup.hong@yonsei.ac.kr) | Sungeun Yang (syang@kist.re.kr)

**Received:** 21 May 2025 | **Revised:** 27 September 2025 | **Accepted:** 22 October 2025

**Keywords:** alloy catalyst | carbon deposition | $CO_2$ electrolysis | electrochemical $CO_2$ conversion | solid oxide electrolysis cells

## ABSTRACT

Electrochemical $CO_2$ reduction using solid oxide electrolysis cells (SOECs) directly converts $CO_2$ into value-added chemicals, mitigating greenhouse-gas emissions. Nickel (Ni) is the conventionally used fuel-electrode electrocatalyst, yet its intrinsic catalytic behavior is underexplored. This study systematically evaluates Ni alloyed with 5 at% Fe, Co, or Cu for changes in microstructure, electrochemical activity, and carbon coking resistance. Model electrodes fabricated by pulsed laser deposition are analyzed by scanning and transmission electron microscopy, X-ray diffraction, and X-ray absorption spectroscopy, which confirm homogeneous alloy formation and show that additive metals modulate active site density by modulating sintering behavior, thereby tuning the triple-phase-boundary density in the order Ni > Ni–Cu > Ni–Co > Ni–Fe. Electrochemical impedance spectroscopy reveals that the apparent activation energy ($E_a$) related to surface reaction decreases for all samples, accelerating $CO_2$ electrolysis, while sensitivity to the $CO/CO_2$ ratio rises when the alloying element is less prone to $CO_2$ dissociation. Diffuse reflectance Fourier-transform infrared spectroscopy and density functional theory calculations indicate that Co and Fe facilitate $CO_2$ dissociation, whereas Cu facilitates fast desorption of product species and enhances turnover activity. Cu alloying markedly suppresses carbon coking, whereas Co exacerbates it. Enhanced performance and durability are validated by impedance and Galvano-static measurements. These findings demonstrate that Ni–Cu alloy electrodes offer a practical route to boost SOEC efficiency and mitigate coking with minimal structural change.

## 1 | Introduction

Electrochemical $CO_2$ conversion is one of the most prominent carbon capture and utilization (CCU) technologies for mitigating climate change. As $CO_2$ emissions are a primary driver of global warming, achieving net-zero carbon emissions has become increasingly urgent. Consequently, CCU strategies focus not only on capturing $CO_2$ but also on converting it into valuable products, thereby creating economically viable solutions [1, 2]. Among various CCU approaches, electrochemical conversion stands out due to its ability to directly transform $CO_2$ into high-value-added products through highly efficient electrochemical reactions [3]. Furthermore, coupled with renewable energy sources, electrochemical $CO_2$ conversion offers a sustainable pathway for carbon utilization, contributing to net-zero goals and addressing the challenges posed by climate change [4].

Low-temperature and high-temperature electrolysis are two major pathways for electrochemically converting $CO_2$ into valuable products. While the low-temperature electrolysis can produce complex chemical substances, it still suffers from low selectivity and efficiency. Meanwhile, high-temperature electrolysis, particularly using solid oxide electrolysis cells (SOECs), has drawn attention due to its superior efficiency and selectivity in producing simple chemicals like CO and $H_2$ [3, 5]. Among these, the direct production of CO from $CO_2$ in an SOEC (hereafter $CO_2$-SOEC) is especially attractive. In addition to its inherent economic value, CO can also serve as a chemical feedstock, replacing conventional carbon sources in petrochemical methods [2], potentially even enabling net-negative carbon emissions [4]. Several studies underscore the potential of using CO from direct $CO_2$-SOECs in producing various synthetic fuels, including methane [6], methanol [7, 8], and aviation fuel [9, 10], highlighting their role in transitioning to sustainable energy systems [5, 11–13]. However, $CO_2$ electrolysis still faces challenges to fully realize these benefits—especially the fuel electrode.

The primary challenge in $CO_2$-SOECs is developing a fuel electrode that efficiently converts $CO_2$. Because the electrolyte and air electrode are largely adopted from the well–developed $H_2O$-SOEC platform, research has concentrated on tailoring the fuel electrode to the unique demands of $CO_2$ conversion. A fuel electrode for $CO_2$-SOEC should overcome the strong thermodynamic stability of the $CO_2$ molecule, which imposes a high activation-energy barrier [5], and prevent carbon coking at the electrode, whereby deposited carbon blocks active sites or even fractures the cell [14]. To address these issues, various strategies have been explored, including infiltration of additional catalysts such as ceria-based [15–19] or metal catalyst [20–23] to Ni/YSZ electrodes, a combination of ceria and metals for synergistic effects [24–27], and even alternative oxide-type electrodes [28–31]. These approaches primarily focus on increasing the number of active sites, whereas direct modification of the intrinsic catalytic properties of Ni in the cermet has received relatively little attention.

Alloying represents a promising route to tune the intrinsic activity of Ni catalysts, yet prior efforts have largely relied on infiltration or exsolution techniques. Infiltration introduces additional metals onto a Ni/YSZ scaffold, effectively enhancing TPB density but not yielding homogeneous Ni–M alloys. Exsolution, in contrast, generates alloy nanoparticles from oxide-based scaffolds such as perovskites, thereby departing from the conventional Ni/YSZ cermet architecture. While both methods can improve performance, they do not directly isolate the effect of alloying within the Ni/YSZ framework.

In heterogeneous catalysis, such as in an SOEC, where reactions occur between a solid catalyst and gas-phase molecules, binding energy is a pivotal factor determining overall reactivity [32]. A good electrocatalyst should not bind reaction intermediates too strongly or too weakly [33], a concept known as the Sabatier principle. Several studies have indicated that alloying, a conventional approach for tuning heterogeneous electrocatalytic properties, is a promising strategy for enhancing the activity of electrocatalysts [34–36]. Specifically, alloying can alter the electronic structure and shift the D-band center, thereby affecting the reaction kinetics [37, 38]. Moreover, local strain induced by a different lattice parameter between the host and the added atom can either promote or hinder the reaction [35, 39, 40]. We, therefore, anticipate that employing an alloying strategy could likewise prove highly beneficial for Ni-YSZ cermet electrodes, leveraging the same principles of electronic and structural tuning.

Computational studies using density functional theory (DFT) suggest that Fe and Co exhibit better reactivity than Ni for $CO_2$ electrolysis, whereas Cu shows lower performance [41–43]. Notably, experimental results also indicate that Fe-based electrodes can outperform Ni-based ones in $CO_2$ electrolysis, likely due to the high oxophilicity of Fe; however, Fe's susceptibility to oxidation raises stability concerns [44]. Conversely, experimental studies report improved electrochemical activity with Ni–Cu alloys [45] or Cu nanoparticles [46] under specific oxide-anode configurations, highlighting discrepancies between theoretical predictions and experimental outcomes.

In terms of carbon coking resistance, several studies have shown that Cu–Ni alloys enhance carbon coking resistance by lowering carbon adsorption energy [47–51], while Co-Ni alloys can exhibit variable resistance depending on cobalt content [52–54]. As for Fe–Ni alloys, partial oxidation of Fe provides oxygen to deposited carbon, thereby mitigating coke formation [55, 56]. Although these alloy-based approaches have demonstrated carbon coking resistance [20, 22, 23, 25, 57–59], comparative data under equivalent conditions remain scarce, hindering the identification of optimal alloying elements and key performance parameters. To the best of our knowledge, no prior study has systematically compared the electrochemical activity and carbon coking resistance of Ni alloys with Cu, Fe, and Co while preserving the same Ni/YSZ cermet structure and evaluating them under identical $CO_2$-SOEC conditions. While previous reports have typically examined only one or two alloying cases in isolation, our work provides a comprehensive comparison across multiple alloying elements, focusing on earth-abundant first-row late transition metals (Fe, Co, Ni, Cu) under consistent conditions with homogeneous alloying conditions. This approach allows us to isolate the intrinsic impact of alloying from other morphological or microstructural variables.

In this study, we systematically investigated Cu-, Fe-, and Co-alloyed Ni/YSZ electrodes, which were fabricated by pulsed laser deposition (PLD) to precisely control composition and microstructure. X-ray diffraction (XRD), transmission electron microscopy (TEM), and X-ray absorption spectroscopy (XAS) elucidated structural, chemical, and morphological changes induced by alloying. Electrochemical impedance spectroscopy (EIS) was conducted to characterize the intrinsic electrochemical activity of the Ni–M/YSZ electrodes, while carbon coking resistance was assessed by exposing the electrodes to a $CO_2$/CO gas mixture and analyzing carbon deposition both quantitatively and qualitatively. Moreover, diffuse reflectance Fourier transform infrared (DRIFT) spectroscopy and computational approach using density functional theory (DFT) were employed to elucidate the catalytic properties relevant to electrochemical activity and coking resistance. Through this comprehensive approach, we clarify how Fe, Co, and Cu alloying

influences both performance and structure of the electrodes, ultimately identifying the most effective alloying strategy, Ni–Cu, for high-performance and durable $CO_2$-SOEC fuel electrodes.

## 2 | Results and Discussion

### 2.1 | Structural and Morphological Characterization of the Samples

Alloying is a promising strategy for enhancing the performance of Ni-based cermet electrodes in $CO_2$-SOEC, offering improvements in catalytic activity and carbon coking resistance. While Ni-YSZ is widely recognized as an effective fuel electrode, its performance can be further optimized through alloying. Previous studies have reported alloying strategies for the $CO_2$ electrolysis reaction. For instance, Ni–Cu alloys formed through exsolution on oxide electrode systems have demonstrated better performance than Ni exsolved only [45]. Additionally, Ni–Fe alloys have been explored on the LSFN electrode, also exhibiting promising results [60]. However, comprehensive studies systematically comparing the effects of different alloying elements on Ni/YSZ cermet under equivalent conditions remain limited. To address this gap, we systematically investigated the influence of alloying elements on the electrochemical properties, including the morphological aspects of Ni/YSZ electrodes.

Model electrode samples were fabricated using the pulsed laser deposition (PLD), which provides precise composition control and yields uniform Ni–M (M: Cu, Fe, Co) alloy/YSZ cermet on YSZ substrates. By utilizing PLD, we ensured that the alloying elements were evenly distributed, allowing for a more controlled investigation of their influence on the electrochemical and thermochemical properties of the electrodes. A symmetrical Ni–M/YSZ cermet electrode was formed with a target thickness of 3 μm, resulting in a Ni-cermet structure characterized by hundreds-of-nanometer-sized particles in a percolating network, as confirmed by SEM and TEM analysis (Figure 1A). All samples were subsequently reduced for structural observation.

Homogeneous alloy formation was observed in the HAADF and TEM-EDS mapping images in Figure 1B–D. TEM-EDS mapping analysis confirmed uniform distributions of Cu, Fe, and Co within Ni grains and clear separation from YSZ grains. Small secondary metal particles were observed only for the 5Cu95Ni sample. However, those nanoparticles cannot contribute to the electrode reactions as these particles were non-percolating and thus did not participate in the electrochemical reaction at the triple-phase boundary (TPB).

To gain further insights into the structural properties of the alloyed electrodes, XRD analysis was performed. As shown in Figure 1E, all Ni–M alloy/YSZ samples exhibit clear YSZ and Ni (metal) peaks without secondary peaks corresponding to additive element M (Cu, Co, and Fe) species, indicating that the additive elements did not form separate phases. Rietveld refinement was conducted to determine the lattice parameter of the Ni structure to assess structural change due to alloying. The calculated lattice parameters from each sample, based on Ni FCC structure and the atomic radii of each element, are presented in Figure 1F. The atomic radii of Cu, Ni, Co, and Fe are 140, 163, 192, and 194 pm, respectively. The lattice parameter of Ni decreased slightly for 5Cu95Ni and increased for 5Co95Ni and 5Fe95Ni, reflecting the influence of the atomic radii of additive elements. To further validate these results, HR-TEM combined with FFT analysis was also performed, and the diffraction patterns confirmed that all alloyed samples exhibit a clear FCC structure consistent with the XRD findings (Figure S1). This provides additional evidence for the homogeneous formation of the Ni–M alloys in our samples.

The homogeneity of the alloys was further corroborated through XAS analysis. Co K-edge and Fe K-edge analyses (Figure 1H; Table S2) revealed that the additive metals, Co and Fe, were alloyed with Ni, leading to shortened bonding lengths compared to their respective reference foils. The bonding lengths of Ni–Co (2.479 Å) and Ni–Fe (2.482 Å) in the alloy sample were reduced relative to the bonding lengths of Co–Co (2.493 Å) and Fe–Fe (2.516 Å) obtained from respective metal foils. Additionally, the shape of the XANES spectra remained consistent across samples (Figures 1I,J and S1), reflecting structural similarity that aligns with the FCC structure of the Ni matrix [61–63], which constitutes the majority of the alloy. Furthermore, the edge of the XANES region exhibited a blue shift (Figure 1I,J), suggesting that the oxidation state of Co and Fe in the samples was higher than that in the reference metal foils [64–67]. This shift indicates electron donation from Co and Fe to Ni, reducing the electron density of the additive metals. Although the Cu *K*-edge was also investigated, analysis was precluded due to the overlap of the Ni *K*-edge signal with the XANES region of the Cu *K*-edge. TEM-EDS, XRD, EXAFS, and XANES analyses confirm that the structure of Ni in Ni–M/YSZ electrodes maintains an FCC structure with homogeneous alloying of the secondary metals.

Owing to the ability of the additive metals to act as a sintering aid and influence the electrode structure, we investigated the morphological characteristics of the electrodes. According to the previous literature, Co and Fe are known to act as effective sintering aids and increase the particle size in Ni/YSZ systems [68]. During our sample preparation, the Ni–M/YSZ electrodes underwent sintering at 1200°C after pulsed laser deposition to form a stable cermet composite microstructure, which explains the different particle sizes observed in Figure 1G and Supplementary Figure S4, which display SEM images of the samples.

These differences in sintering behavior likely affect the TPB length and, in turn, influence the electrochemical performance of the electrodes. To quantitatively analyze the morphological characteristics, image analysis was conducted based on TEM images. The Ni (or Ni–M alloy) particle sizes were measured as $143.21 \pm 34.16$ nm for Ni(ref), $162.5 \pm 48.07$ nm for 5Cu95Ni, $173.96 \pm 35.46$ nm for 5Co95Ni, and $187.81 \pm 47.62$ nm for 5Fe95Ni, as shown in Figure 1G. The YSZ particle sizes also exhibited a similar growth trend. Overall, the metal additives increased particle size, with the 5Fe95Ni sample exhibiting a 31% growth compared to the Ni(ref) sample. The corresponding particle size distributions and statistical parameters are provided in Figure S2. These differences in sintering behavior likely

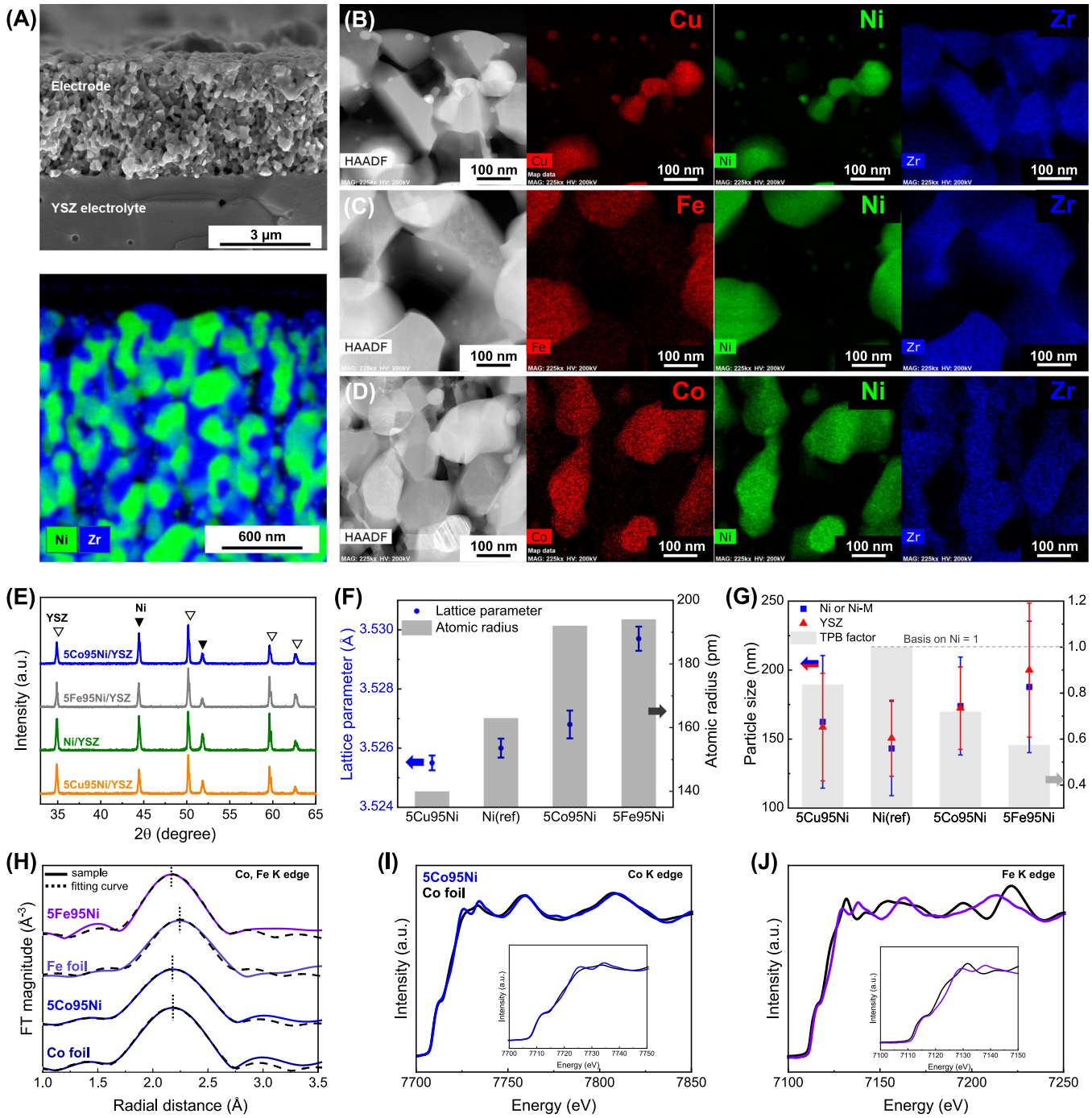


**FIGURE 1** | (A) SEM images of the Ni/YSZ electrode along with an TEM-EDS mapping image. (B–D) HAADF-STEM and TEM-EDS mapping images of the Ni–M/YSZ electrodes (M = Cu, Co, Fe). E) XRD patterns of reduced Ni–M/YSZ electrodes. (F) Lattice parameter of the metallic phase obtained by Rietveld refinement, shown with the atomic radius of Ni and the alloying elements. (G) Ni particle sizes and normalized TPB factors of each sample. (H) Fourier transform spectra of 5Co95Ni/YSZ and the normalized XANES spectra of (I) Co and (J) Fe with reference metal foils. 5Fe95Ni/YSZ, and foils.

influenced the TPB length, which directly correlates with the electrochemical performance of the electrode.

The TPB lengths were calculated based on the particle sizes shown in Figure 1G, leveraging the inverse proportionality between TPB length and particle size [69–71]. To compare the samples, we introduced the TPB factor, defined as the reciprocal of the product of the Ni–M and YSZ particle sizes, normalized relative to the factor of Ni(ref). The TPB factors were calculated as 0.84 for 5Cu95Ni, 0.45 for 5Co95Ni, and 0.55 for 5Fe95Ni, indicating that the metal additives used for alloying reduced the TPB by up to 45%. Among the added metals, Cu caused the smallest increase in particle size, making Cu an ideal choice for maintaining a longer TPB length. This characteristic is crucial for achieving high-performance electrochemical cells and underscores the importance of considering morphological variations when designing electrodes with alloying strategies.

## 2.2 | $CO_2$ Reaction Mechanism Study With Electrochemical Impedance Spectrum Analysis

The electrochemical activity of the Ni–M/YSZ electrode under $CO_2$/CO atmosphere was evaluated using symmetrical cells, which were composed of two identical Ni–M/YSZ electrodes deposited by pulsed laser deposition on an electrolyte (YSZ). Although Ni/YSZ is widely recognized as a highly active fuel electrode in SOECs, previous studies have predominantly focused on oxide-type fuel electrodes or the incorporation of additional catalysts to enhance performance under $CO_2$/CO conditions [15, 28–31, 45, 60, 72]. However, there remains a distinct lack of research investigating the homogeneous alloying of Ni with other metals for $CO_2$ electrolysis applications based on Ni/YSZ.

In the $CO_2$ reduction process, the reaction proceeds via the cleavage of $CO_2$ to form CO and a surface-bound oxygen species, followed by the desorption of CO from the catalyst surface, as depicted in Figure 2A. To understand how the Ni–M/YSZ electrodes facilitate these steps, we conducted electrochemical impedance spectroscopy (EIS) analysis under open-circuit voltage (OCV) conditions. The Nyquist and Bode plots depicted in Figure 2B–E were measured at 800°C and 650°C under an 80% $CO_2$ atmosphere for each sample. It reveals the presence of two representative reaction resistances, with peaks occurring in the frequency ranges of 1–10 Hz, low-frequency (LF), and 100–1000 Hz, high-frequency (HF), across all temperatures.

In the Ni/YSZ electrode, the LF resistance is related to gas diffusion within the pore structure [73] of the electrode or the thermochemical gas conversion reaction [74]. Since no thermochemical gas conversion reaction is expected under $CO_2$/CO conditions, the LF resistance can be attributed to gas diffusion [75, 76]. The HF resistance is reported to be associated with the

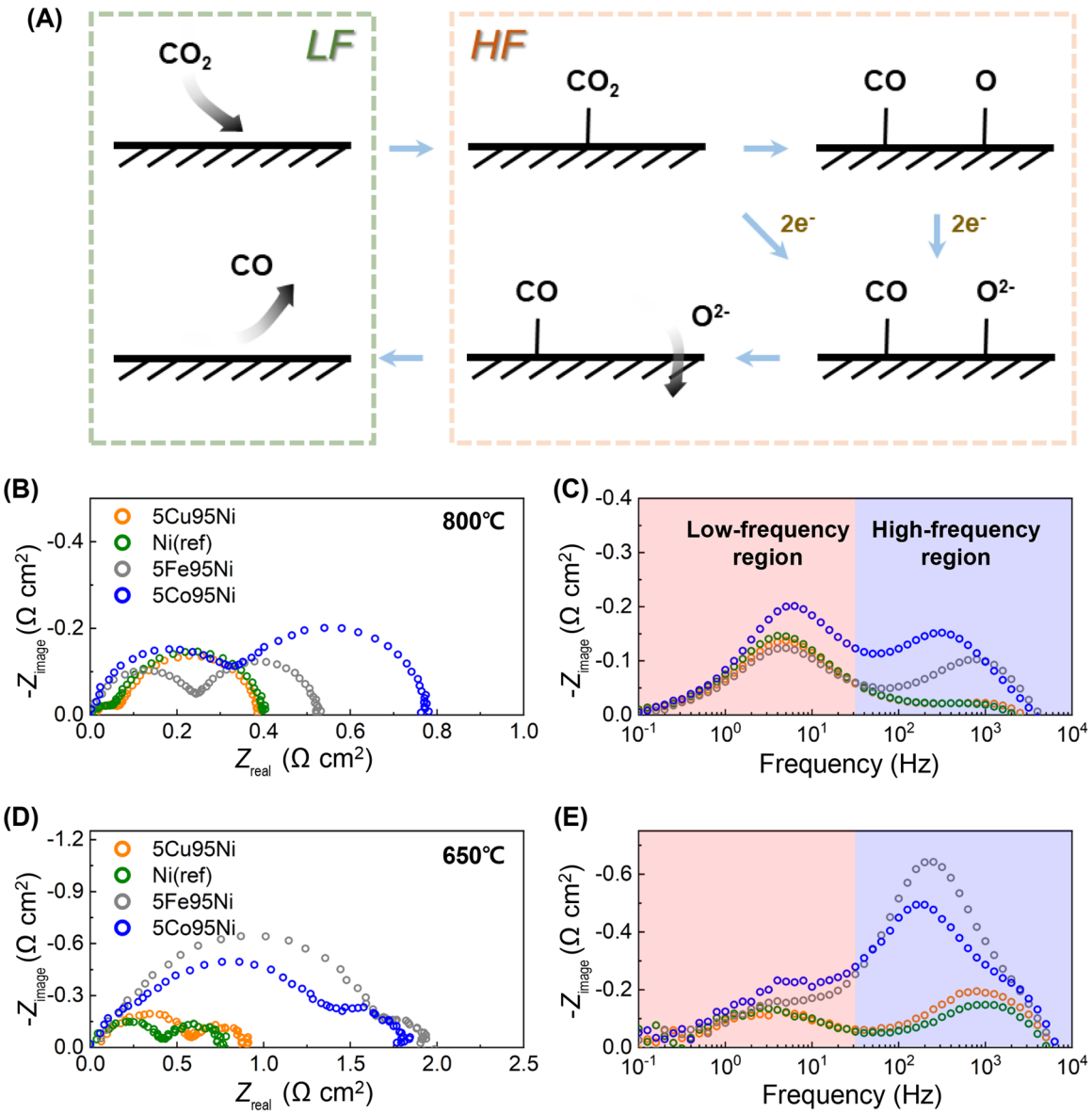


**FIGURE 2** | (A) Schematic illustration of $CO_2$ reduction reaction. Nyquist and Bode plot under $CO_2$/CO (80:20) atmosphere at different temperatures. (B, C) 800°C, (D, E) 650°C represented as (B, D) Nyquist plots, and (C, E) Bode plots.

charge transfer reaction, including the conversion of neutral species to ions or vice versa [74, 77–79]. Specifically, for $CO_2$ electrolysis, both dissociative $CO_2$ adsorption and charge transfer processes at the fuel electrode refer to this frequency range [76, 80, 81]. The dissociative adsorption of $CO_2$ is known to be the rate-determining step (RDS) among the elementary steps of the $CO_2$ electrolysis reaction. The variation in HF resistance among samples is likely related to this step.

To further investigate the temperature dependency of the resistances, an electrical circuit model (ECM) fitting was employed. This fitting allowed us to accurately separate the LF and HF components (Figure 2C,E) and gave valuable insights into the electrochemical activity of each sample, helping to identify the appropriate catalysts under the given conditions. The Arrhenius plot of the two resistances from the analysis is presented in Figure 3A (HF) and B (LF). The LF resistances, Figure 3B, remain similar across different temperatures for all samples, confirming that this resistance is indeed associated with gas diffusion phenomena, which are less affected by changing temperature compared to the surface reaction. On the other hand, the HF resistances, Figure 3A, show a clear temperature dependency and notable differences among the samples, which can be linked to variations in surface reaction kinetics and TPB lengths of the electrodes, as previously mentioned, due to the alloying and sintering aid effect.

The two types of resistance exhibit clearly different temperature behaviors, indicating that the electrode must be optimized in different ways depending on the operating temperature. At high temperatures, the HF resistance becomes smaller because it is strongly temperature-dependent, making LF resistance (gas diffusion) account for a larger portion of the total resistance. A summary of the HF resistance ratios is provided in Table S4, which clearly demonstrates the reduction in HF contribution with increasing temperature. For instance, in the Ni(ref) sample, the HF resistance decreases from 74% to 78% at 650°C to 29%–41% at 800°C. This highlights that, under high-temperature operation, improving gas diffusion through electrode structure optimization is critical. Conversely, at lower temperatures, such as 650°C, HF resistance dominates because catalytic activity is reduced. Therefore, enhancing the catalytic activity of the electrode becomes the key strategy to achieve better performance in low-temperature operation.

The quantitative values of the HF resistance, surface reaction, vary significantly among the samples (Figure 3A). The highest HF resistance is observed in 5Co95Ni, followed by 5Fe95Ni,

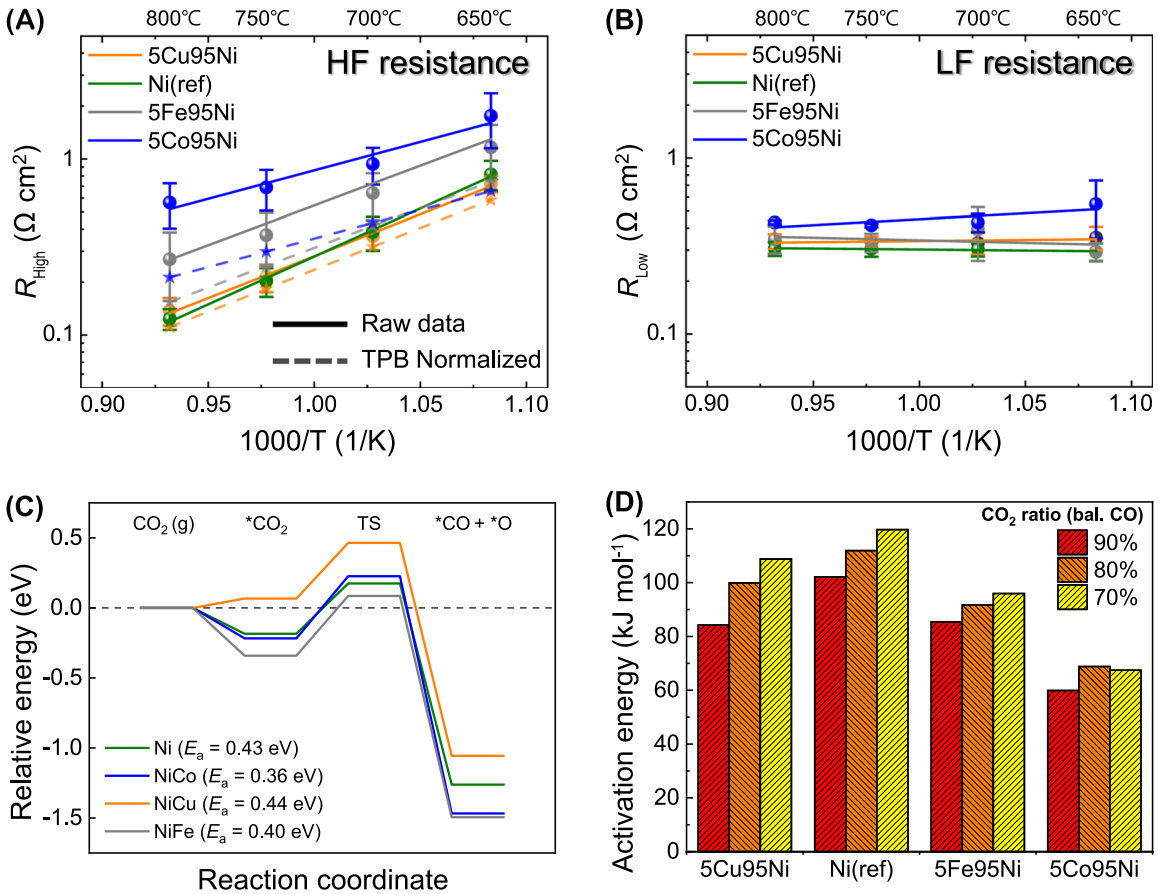


**FIGURE 3** | Arrhenius plot of resistance at $CO_2$/CO (80:20) atmosphere. The linear lines in the graph represent the mean values at each temperature; data points in (A) and (B) include error bars showing the standard deviation from three independent measurements. (A) High-frequency resistance (dotted line is normalized resistance by TPBs). (B) Low-frequency resistance. (C) Reaction profile of $CO_2$ reduction on Ni(111), Co-doped Ni(111), Cu-doped Ni(111), and Fe-doped Ni(111). (D) Apparent activation energy calculated from high-frequency resistance at different $CO_2$ ratios.

while 5Cu95Ni and Ni(ref) show similarly low values. As previously discussed, the TPB length varies significantly among the samples, which can influence the overall resistance. To account for this variation, Figure 3C presents the normalized HF resistances using the TPB factors calculated earlier (Figure 1C), enabling a comparison of the samples with similar TPB lengths to the Ni/YSZ reference sample. This normalization allows for a direct comparison of electrodes. The results show that all samples fall within a similar range after normalization, confirming that TPB length plays an important role in influencing the overall magnitude of the resistance. Even after TPB normalization, 5Cu95Ni consistently exhibits the lowest resistance, indicating that Cu alloying can yield the highest-performing electrode.

The intrinsic catalytic property was further examined through the apparent activation energy calculated from temperature-dependent HF resistance, as shown in Figure 3D. The results reveal that 5Co95Ni exhibits the lowest apparent activation energy, followed by 5Fe95Ni, 5Cu95Ni, and Ni(ref). The low apparent activation energy of 5Co95Ni and 5Fe95Ni can be explained by the high activity of Co and Fe for $CO_2$ dissociation. Although Cu is considered less favorable for $CO_2$ dissociation, the 5Cu95Ni alloy displays higher activity than Ni(ref) in our results. This can be attributed to weaker CO adsorption [82], leading to a more efficient turnover of the reactive sites [49].

An interesting trend was observed: apparent activation energy tends to decrease as the $CO_2$ ratio increases for all samples (Figure 3D). This indicates that the reaction step is very sensitive to the CO2 partial pressure; in other words, the rate-determining step involves gaseous CO2. This trend is more pronounced in 5Cu95Ni, while 5Fe95Ni and 5Co95Ni exhibit less dependency. These trends are associated with the relationship between apparent activation energy and surface coverage [83, 84]. This means that when the dissociation step is more difficult, such as for Cu, it becomes more affected by changes in the partial pressure of the reactant, leading to differences in the surface coverage of reaction intermediates. This strengthens our hypothesis that the $CO_2$ activation step is facilitated by alloying Ni with Fe and Co, which provide strong adsorbing surfaces for $CO_2$, while the step was hindered by alloying Ni with Cu, which creates a weaker adsorbing surface for $CO_2$.

The alloying effect was further examined with DFT calculations. We investigated adsorption and dissociation of $CO_2$ on a Ni(111) surface in which the topmost layer was doped with an additional metal, simulating 5% alloying used in the experiments. The calculated activation barriers follow the order of Co-doped Ni(111) < Fe-doped Ni(111) < pure Ni(111) < Cu doped Ni(111) (Figure 3C, detailed steps in Figure S7), closely resembling the apparent activation energies observed in the experiments (Figure 3D). $CO_2$ adsorption energies also follow the same trend: they increase with Co and Fe doping but decrease with Cu doping (Figure S6, Table S3). Additionally, the CO adsorption energy was calculated with different dopant concentrations (Figure S8). Notably, the adsorption energy of CO was decreased with the increase in Cu doping ratio. This behavior implies that Cu promotes faster CO desorption from the Cu-doped Ni surface, potentially contributing to improving the apparent catalytic activity for entire $CO_2$ reduction reaction.

## 2.3 | In Situ Drift Analysis of $CO_2$ Surface Intermediates in Ni–M Catalysts

From the previous analysis, we observed that the apparent activation energy varies with the $CO_2$/CO ratio, suggesting its connection to catalytic surface properties. Additionally, the results indicate that the rate-determining step involving $CO_2$ is influenced by the alloying elements. To support these findings and further investigate the catalytic surface interactions, we conducted in situ diffuse reflectance FT-IR (DRIFT) analysis to examine surface reaction intermediate species on the catalysts in a working atmosphere, with temperature ranging from 200°C to 400°C under 10% $CO_2$ in Ar balance flow (Figures 4 and S9).

The charge transfer reaction in $CO_2$ electrolysis involves several steps (Figure 2A). First, $CO_2$ adsorbs onto the surface and dissociates into *CO and *O, which is the most energy-intensive step. The *CO then desorbs as a product gas, while the remaining *O diffuses to the TPB and enters the electrolyte after the charge transfer reaction to $O^{2-}$. Meanwhile, $*CO_3$ can also form on the surface, either by an *O atom attaching to $*CO_2$ or by two *O atoms attaching to *CO, and this carbonate species can occupy the surface sites. The formation of $*CO_3$ could potentially hinder the desired electrolysis reaction by reducing the surface vacancy fraction ($\theta_V$), thereby limiting the availability of sites for the adsorption of desired intermediate species [85].

The observed peaks in the IR spectra were assigned to specific vibrational modes of surface carbonate species. The peaks at 1622 and 1430 $cm^{-1}$ correspond to the asymmetric and symmetric stretching of bicarbonate [86–88]. The peaks at around 1490 and 1370 $cm^{-1}$ are attributed to the asymmetric and symmetric stretching of monodentate carbonate [89, 90]. Additionally, the peak at 1225 $cm^{-1}$ is assigned to the bending mode of OH in bicarbonate [86–88]. The adsorbed *CO peak appears near 2070 $cm^{-1}$ [91, 92] and gaseous $CO_2$ peaks were observed at around 2350 and 675 $cm^{-1}$ [93, 94]. However, as shown in Figure S9, in contrast to the $*CO_3$ peaks, no meaningful difference was observed from the *CO peaks due to the resolution limitations. Furthermore, the adsorbed $CO_2$ peaks ($*CO_2$) typically require extremely low temperatures for observation [94] and, therefore, are not detected in our measurements. Consequently, the analysis focused on the distinct changes in $*CO_3$ peaks, where pronounced differences were apparent depending on the alloy composition.

To further investigate the relationship between the different alloys and surface reaction intermediate, the change in $*CO_3$ peaks under a $CO_2$ atmosphere at temperatures ranging from 200°C to 400°C is presented in Figure 4. At 200°C, the intensity of the $*CO_3$ peaks followed the order of 5Cu95Ni, 5Fe95Ni, and 5Co95Ni. The decrease in peak intensity as the temperature increased varied significantly between the samples. The higher $*CO_3$ intensity observed in the 5Cu95Ni sample, compared to the remarkably lower intensity in the 5Co95Ni sample, can be explained as follows: a higher $*CO_3$ peak of the

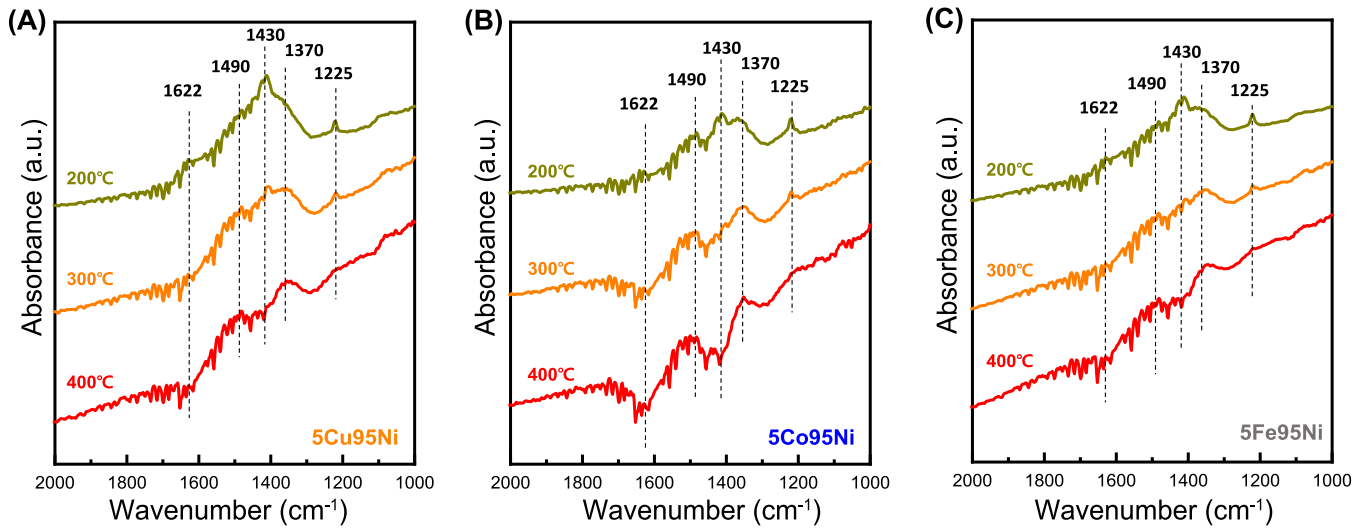


**FIGURE 4** | In situ DRIFT spectra in $CO_2$ atmosphere at 200°C to 400°C of various samples. (A) 5Cu95Ni, (B) 5Co95Ni, and (C) 5Fe95Ni.

5Cu95Ni indicates a reduced amount of $CO_2$ dissociation, which is associated with a higher apparent activation energy among the alloyed catalysts. In contrast, the lower $*CO_3$ intensity in the 5Co95Ni sample suggests that $CO_2$ dissociation is more favorable than the formation of $*CO_3$, leading to lower apparent activation energy. These observations are consistent with the electrochemical activity we observed in the previous section.

The DRIFT analysis shows that the $*CO_3$ intensity increases in the order of Co, Fe, and Cu, consistent with their tendencies for $CO_2$ dissociation calculated by DFT (Figure 3E). This order aligns with the differences observed in apparent activation energy and $CO_2$/CO composition dependence (Figure 3C,D), highlighting that alloying with Co shows the most efficient $CO_2$ dissociation, followed by Fe and then Cu. These results suggest that alloying influences the formation and coverage of surface intermediates, directly impacting the electrochemical performance. However, stronger $CO_2$ dissociation alone does not necessarily translate into superior overall activity, since CO desorption and carbon coking must also be considered. Catalysts that efficiently split $CO_2$ may also prevent CO desorption and accelerate CO decomposition, increasing the likelihood of residual carbon formation.

According to the Sabatier principle, optimal catalytic performance is achieved when adsorption strength is balanced—neither too strong nor too weak. Cu alloying illustrates this balance. While DRIFT and DFT analyses confirm that Cu weakens $CO_2$ adsorption, DFT further shows that the CO adsorption energy decreases with increasing Cu doping (Figure S8). Although such Cu segregation at the surface was not experimentally observed in this study, this computational result suggests a possible mechanism by which Ni–Cu alloys may facilitate faster CO desorption and show increased activity. Because the electrochemical reaction product *CO must ultimately desorb as CO(g) to complete the overall reaction, this step could be related to the lower apparent activation energy observed for Ni–Cu alloys compared with the Ni reference (Figure 3D). Moreover, the relatively weaker $CO_2$ dissociation associated with Cu may contribute to reduced *C surface coverage, thereby potentially enhancing carbon coking resistance, which is explored further in the following section.

## 2.4 | Carbon Coking Behaviors in Ni–M/YSZ Electrodes

Carbon coking represents a significant challenge in the $CO_2$ electrolysis reaction, as carbon blocks active sites, leading to a loss of catalytic activity and potential cell failure due to cell fracture. Alloying strategies to mitigate carbon coking have been studied in various catalyst applications, including co-electrolysis (Co-EC) [20–22], steam reforming of methane (SRM) [95–97], and dry reforming of methane (DRM) [98–102]. However, their application in $CO_2$-EC remains completely unexplored. It is expected that alloying could offer comparable benefits in $CO_2$-EC in terms of mitigating carbon coking. In the following section, we investigate how alloying influences coking resistance.

To investigate the coking behavior in Ni–M/YSZ electrodes, we exposed the samples to a gas mixture of $CO_2$/CO (40:60) at 650°C, varying the exposure times, as this condition ensures the formation of coke. In $CO_2$/CO mixtures, carbon coking typically occurs through the Boudouard reaction [103, 104], where two CO disproportionate into $CO_2$ and solid carbon. As the fraction of CO in the gas mixture increases, coking becomes more favorable. At lower temperatures, this effect can be further pronounced, accelerating the coking behavior [105, 106]. We note that in our experimental design, we focused on thermochemical carbon coking to assess the impact of the different alloy catalysts in our samples, as we anticipate that the trend will nevertheless be the same with electrochemical carbon coking.

The deposited carbon on the samples was evaluated using microscopy to observe the surface change. Compared to the samples reduced in an $H_2O/H_2$ mixture in 20 h (Figure 5A–D), black spots emerged on the surface when exposed to the $CO_2$/CO mixture for 5 h (Figure 5E–H). SEM images of black spot and corresponding Raman spectra are depicted in Figure 5I, M,

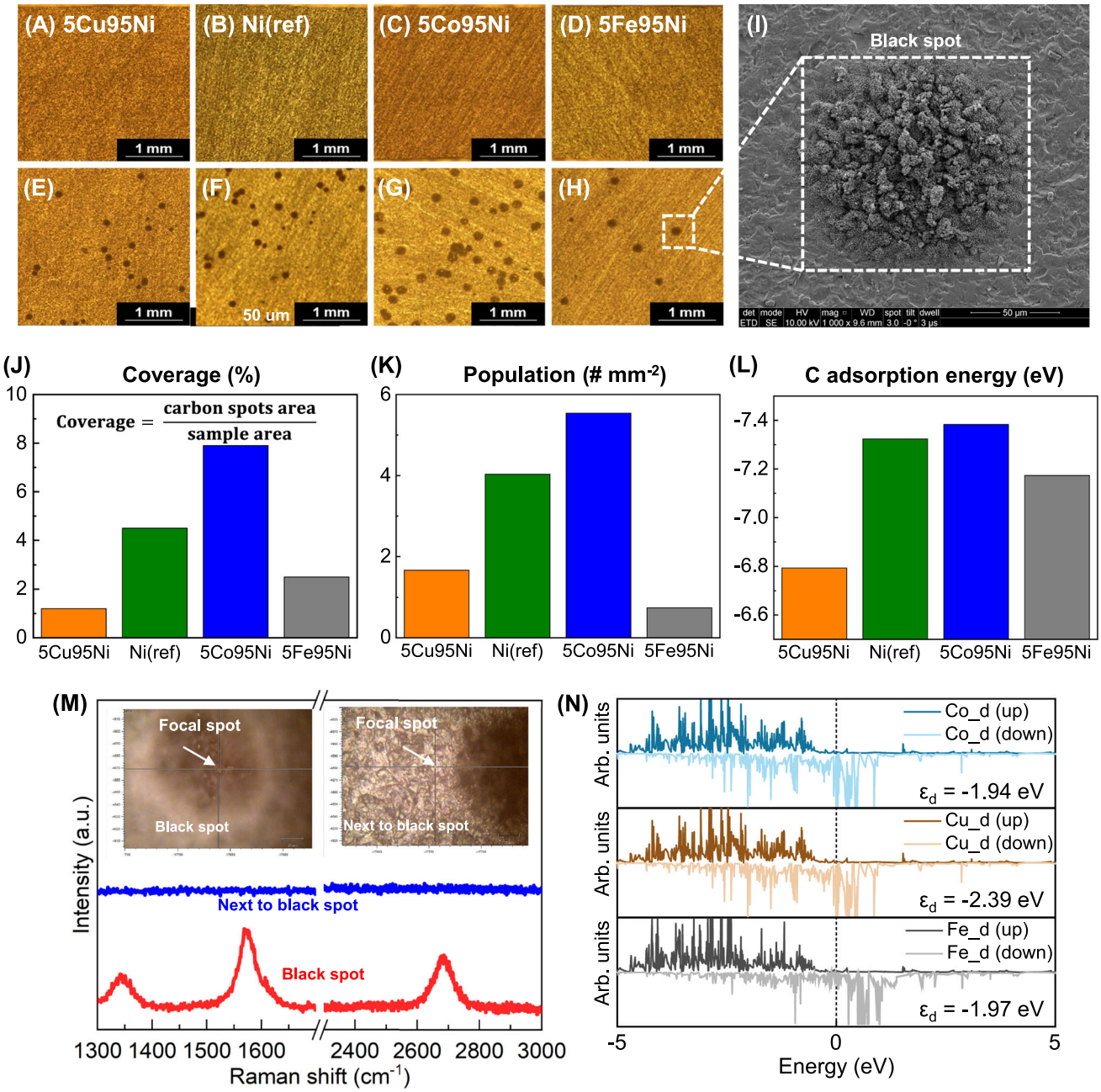


**FIGURE 5** | Optical images of samples treated within different conditions. (A–D) $H_2$ 80%/$H_2O$ in 800°C for 20 h, (E–H) $CO_2$/CO (40:60) in 650°C for 5 h. (I) SEM images of 5Cu95Ni sample. (J, K) Quantitative metrics of 5 h exposed samples. (J) Surface coverage ratio and (K) numbers of the spots per unit area of each samples (Population). (L) DFT-Calculated adsorption energy of C on surface models. (M) Raman spectra of black spot and nonblack spot areas. (N) Projected d-orbital density of states (PDOS) of the dopant atoms (Co, Cu, and Fe) at the surfaces.

which clearly indicates the existence of carbon. Despite the small amount of additional metal, 5% of the Ni, the effect was distinct. After 5 h of exposure, the 5Co95Ni sample showed the most severe coking compared to the Ni(ref) sample, while the 5Fe95Ni and 5Cu95Ni samples showed significantly smaller amounts of coking, indicating that Fe and Cu inhibited the formation of coke, whereas Co increased carbon coking. However, after 10 h of exposure, all samples except for 5Cu95Ni were completely covered with carbon (Figure S10). The results indicate that Cu provides the highest resistance to carbon coking, making it the most stable catalyst for $CO_2$ electrolysis in terms of carbon coking. Additional SEM images at 5, 10, and 15 h are included in Figure S5 to strengthen the evidence for the observed coking behavior and facilitate cross-sample comparison.

To quantitatively analyze carbon coking resistance, we conducted image analysis on the $CO_2$/CO treated samples shown in Figure 5J,K. We measured the surface coverage, which represents the area covered by black spots relative to the total sample area, coverage, (Figure 5J), and the number of spots per unit area, population (Figure 5K). The population increased in the order of 5Fe95Ni, 5Cu95Ni, Ni(ref), and 5Co95Ni. However, the surface coverage was smallest for 5Cu95Ni, followed by 5Fe95Ni, Ni(ref), and 5Co95Ni. The changed order between 5Cu95Ni and 5Fe95Ni is due to the smallest size of the black spots on the

5Cu95Ni sample and the lowest number of black spots on the 5Fe95Ni sample. The consistently high coverage and population on 5Co95Ni confirmed its vulnerability to carbon coking.

Lowering the stability of carbon atoms on a catalyst surface mitigates carbon coking by lowering the possibility of *CO dissociation and allowing surface-adsorbed oxygen species to react more readily with the surface carbon atoms to form CO [107–109]. Therefore, alloying Ni to reduce the binding energy of carbon can enhance carbon coking resistance. To investigate this effect, we calculated the C adsorption energy on each model (Figures 5L and S3). DFT-calculated C adsorption energies were −6.58 eV for Cu doped Ni(111), −6.96 eV for Fe-doped Ni(111), −7.11 eV for pure Ni(111), and −7.17 eV for Co-doped Ni(111). Notably, the presence of Cu significantly lowered the C adsorption energy. It can be explained by the lower D-band center position to the Fermi level of Cu (−2.39 eV) than other Co (−1.94 eV) and Fe (−1.97 eV) at the surface of Ni(111). The D-band electrons near the Fermi level can readily transition to other energy states, thereby facilitating interaction between adsorbate and catalytic surface (Figure 5N) [110]. Therefore, lower D-band center by doping with Cu can effectively reduce the coke formation.

At the early stage (5 h), 5Fe95Ni had the fewest black spots, indicating strong initial resistance to carbon coking compared to other samples. However, once coking initiated, the propagation of these spots proceeded more rapidly than in 5Cu95Ni, resulting in the surface being fully covered by carbon, similar to Ni(ref) and 5Co95Ni, after 10 h (Figure S10). In contrast, the 5Cu95Ni sample remained partially covered. Furthermore, after 1 h of exposure (Figure 6), precipitated nickel particles were observed only in the Ni(ref) and 5Co95Ni samples, whereas no precipitated nickel particles were detected in the 5Cu95Ni and 5Fe95Ni samples. This absence of precipitated nickel in 5Cu95Ni and 5Fe95Ni is likely a key evidence relating to their strong initial resistance to carbon coking. These findings offer qualitative and quantitative confirmation of the prominent carbon coking resistance provided by Cu alloying.

SEM analysis revealed that the black spots (Figure 7A–K) contained carbon nanotubes and amorphous carbon (Figure 7E), which appeared to surround the nickel particles (Figure 7H). SEM-EDS mapping results of the black spot (Figure 7I–K) clearly confirm the presence of carbon. Interestingly, carbon coking was accompanied by significant growth of Ni particles, resulting in particle size much larger than the initial size of 100–250 nm (Figure 1G). Given that the alloying effect could influence the pattern of carbon deposition, Raman spectroscopy was conducted to further investigate these differences. However, no distinct differences were observed between the samples, suggesting that while alloying plays a significant role in the initial stage of carbon deposition, it has a minimal effect on subsequent growth. To gain further insights, we analyzed the D-band and G-band intensity ratio (D/G ratio) of Raman spectra for samples exposed for 5, 10, and 15 h (Figure S8). The results showed similar trends over time, regardless of the sample type, indicating that the progression of carbon growth follows a comparable pattern across all samples.

Previous studies have also reported that the low surface energy of Cu leads to surface enrichment when alloyed with Ni [50, 111–115], blocking the step sites of Ni and further enhancing carbon coking resistance as the Ni step site is more prone to carbon coking [50]. In contrast, the 5Co95Ni sample exhibited higher susceptibility to carbon coking. Studies have

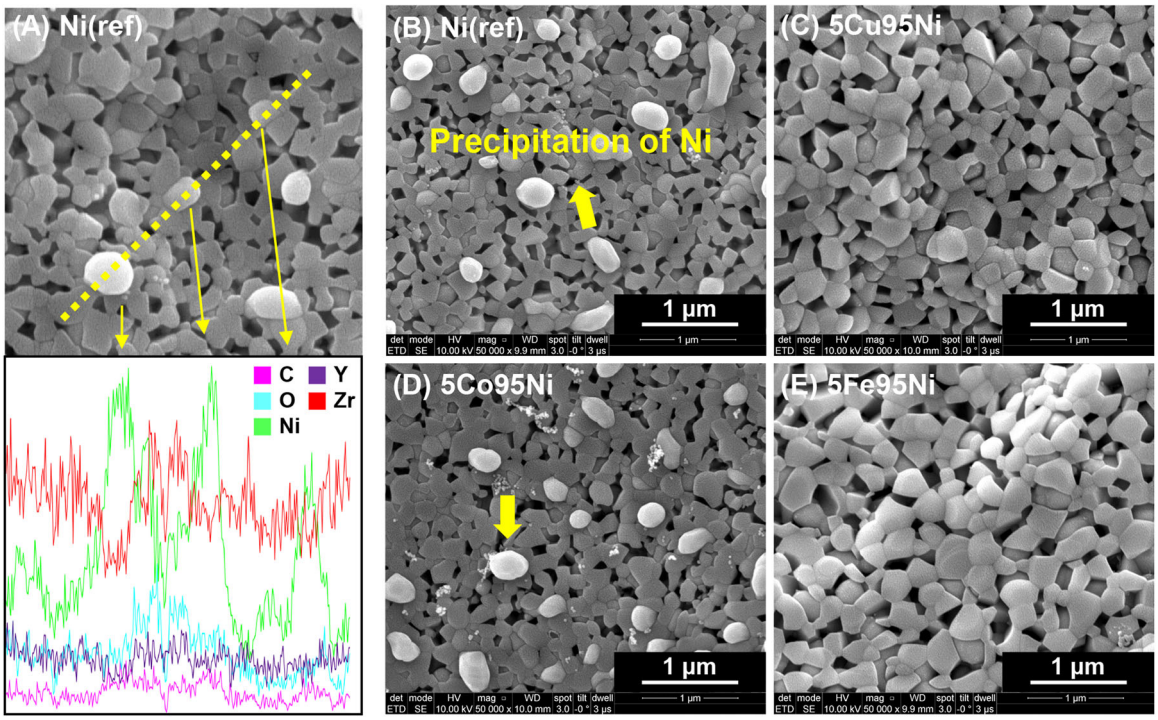


**FIGURE 6** | SEM analysis results of samples treated in $CO_2$/CO (40:60) in 650°C for 1 h. (A) Line scan EDS result of Ni(ref) sample and SEM images of (B) Ni(ref), (C) 5Cu95Ni, (D) 5Co95Ni, and (E) 5Fe95Ni.

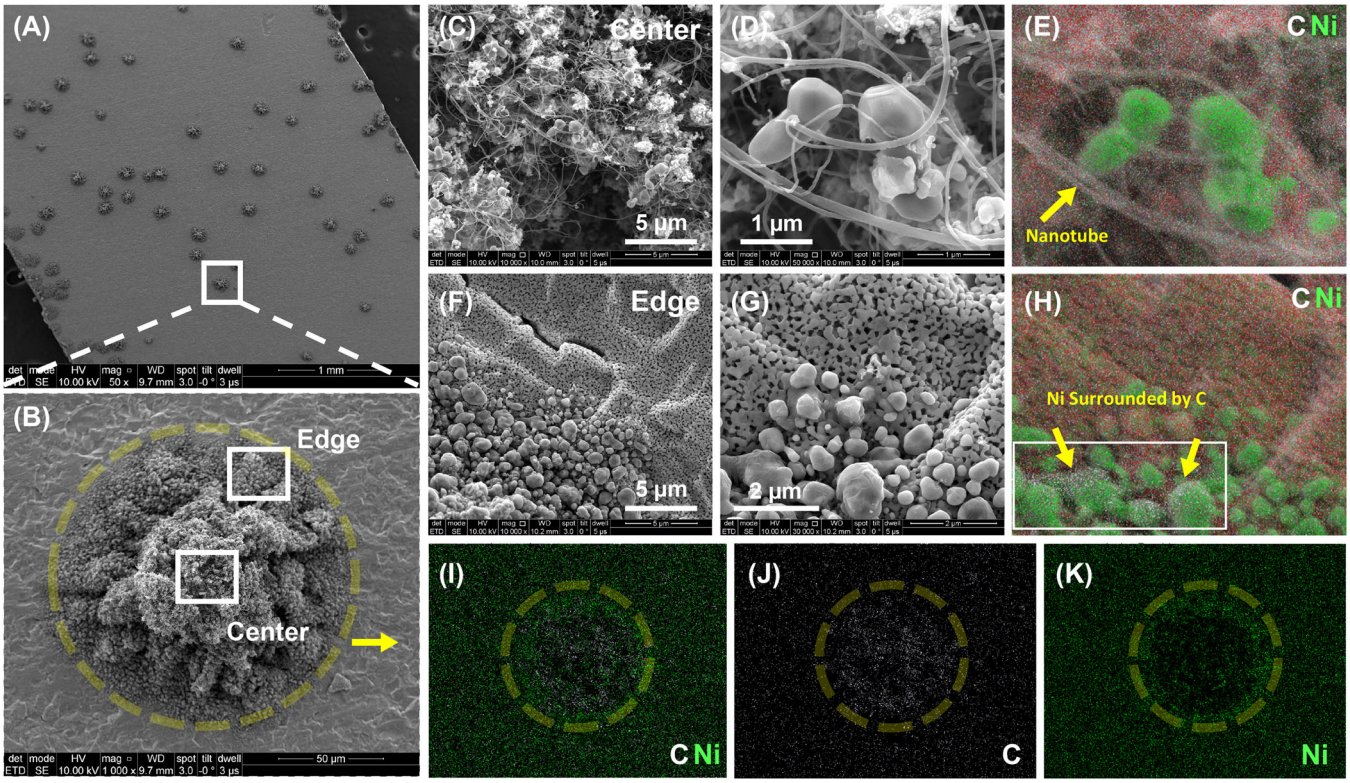


**FIGURE 7** | (A, B) SEM Images of 5 h exposed Ni(ref) samples, (C–E) center of the black spot, (F–H) edge of the black spot, and (I–K) SEM-EDS mapping images of black spot.

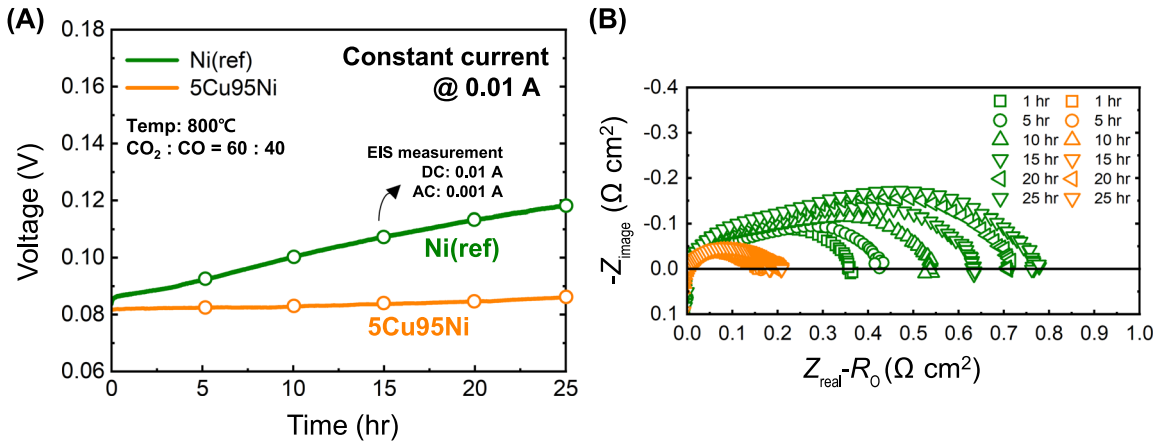


**FIGURE 8** | Electrochemical long-term test results of Ni(ref) and 5Cu95Ni half-cells at 800°C under $CO_2$/CO (60:40). (A) Galvano-static long-term test under 0.01 A for 25 h. (B) EIS results during long-term test.

shown that Co–Ni alloys are more prone to the Boudouard reaction compared to pure Ni. While higher cobalt content improves carbon coking resistance, lower concentrations can lead to rapid deactivation [52–54]. For the 5Fe95Ni sample, the improved coking resistance is likely due to the partial oxidation of Fe, which supplies oxygen to the deposited carbon [55, 56]. This mechanism suppresses coking and potentially contributes to the lowest population value observed in Figure 5K.

To examine the superior carbon coking resistance and catalytic activity of the Cu-alloyed Ni/YSZ electrode under realistic operating conditions with an applied electrical potential, long-term stability tests were performed on 5Cu95Ni and Ni(ref) electrodes, as presented in Figure 8. The substrate thickness was reduced to 80 μm to increase the current density, thereby generating a locally high partial pressure of CO near the electrolyte–electrode interface. In a $CO_2$/CO (60:40) atmosphere at 800°C, galvanostatic operation was carried out under a constant bias of 10 mA, and the cell voltage was monitored over time. In addition, electrochemical impedance spectroscopy (EIS) was measured during the bias condition (Figure 8B) to evaluate performance degradation. The testing condition itself does not generate coke in the absence of current; however, the electrochemical reaction at the interface can increase the local CO concentration, which may lead to carbon deposition.

As shown in Figure 8A, the 5Cu95Ni electrode exhibited higher performance compared to Ni(ref), which is consistent with the lower apparent activation energy shown in Figure 3D. During 25 h of operation, the Ni(ref) samples showed a voltage increase from 0.085 to 0.118 V (~38.8% rise), whereas the 5Cu95Ni sample displayed only a minor change from 0.082 to 0.086 V (~4.8% increase), clearly demonstrating the superior stability of the Cu-alloyed electrode. In addition, EIS spectra collected during the measurement revealed a pronounced increase in polarization resistance for Ni(ref), while the Cu-alloyed electrode showed minimal change (Figure 8B). Specifically, the polarization resistance of 5Cu95Ni increased only from 0.156 to 0.209 $\Omega\,cm^2$ (~34%), while that of Ni(ref) nearly doubled from 0.361 to 0.756 $\Omega\,cm^2$ (~112%). Post-analysis further supported these findings: the Ni(ref) electrode exhibited visible electrode damage after the long-term test, and SEM images confirmed coke formation on the cathodic electrode surface where $CO_2$ reduction occurs, while no such degradation or carbon deposition was observed in the 5Cu95Ni electrode (Figure S12). Together, these results confirm that Cu alloying enhances both catalytic activity and long-term stability by effectively suppressing carbon deposition under realistic electrochemical operating conditions.

In addition to the findings presented above, it is important to address considerations regarding the scalability of the fabrication method and the applicability of the present results to practical SOEC systems. While pulsed laser deposition (PLD) was employed in this study to ensure precise control over electrode composition and microstructure, it is acknowledged that PLD has inherent limitations in terms of scalability for commercial applications. For large-scale manufacturing, adopting similar physical vapor deposition (PVD) techniques—particularly sputtering, which is currently widely used in industrial settings—could offer a more viable pathway. In our recent work, sputtering has been successfully applied to produce $5 \times 5\,cm^2$ thin-film SOFCs [116], with $10 \times 10\,cm^2$ cells under development. Such scalability-oriented fabrication strategies have the potential to bridge the gap between laboratory-scale alloying studies and industrial deployment, thereby accelerating the translation of the present findings into practical $CO_2$-SOEC systems.

Additionally, the experimental configuration used in this study warrants consideration. The symmetrical cell design was chosen as a model system to eliminate multiple variables inherent in practical cells, allowing for a focused evaluation of the intrinsic effects of alloying on the fuel electrode. However, in full SOEC stacks, the air electrode can play a substantial role in determining overall performance alongside the fuel electrode. Moreover, the transport phenomena (e.g., flow field in separator, porous structure in fuel electrode support layer) are known to critically influence both performance and stability [117]. In the context of $CO_2$-SOECs, particularly during low-temperature operation, the partial pressures of CO and $CO_2$ are key factors influencing carbon coking behavior. Consequently, stack- and system-level design factors that govern local gas concentration distribution could play an important role in both electrochemical performance and long-term durability. Future work should therefore extend the present approach to full-cell and stack-level systems under realistic operating conditions, where these additional variables can be systematically evaluated.

## 3 | Conclusion

In this study, we systematically explored how alloying Ni/YSZ electrodes with Cu, Fe, and Co influences electrochemical performance and carbon coking behavior under high-temperature $CO_2$ electrolysis. Although Co alloying significantly reduced the apparent activation energy for $CO_2$ dissociation, leading to higher intrinsic activity, it also introduced notable morphological changes that diminished the overall reactivity and exacerbated carbon coking. By contrast, Cu alloying offered a moderate enhancement in activity while preserving a larger triple phase boundary (TPB) due to minimal particle growth. More importantly, the superior coking resistance of Cu made it a more balanced choice for practical SOEC applications, combining both stable long-term operation and respectable electrochemical performance. These key performance metrics are summarized in Table 1.

Looking ahead, further compositional optimization of Ni–M alloys, beyond the single doping ratio explored here, may unveil synergies or trade-offs that more effectively balance activity and coking resistance. Additionally, advanced electrode microstructure engineering, including graded architectures or refined sintering strategies, could further enhance the performance and stability. By systematically tuning both alloy composition and microstructure features, future investigations can expand on the promising results presented here, driving the development of next-generation SOEC electrodes capable of achieving higher efficiency and durable operation in $CO_2$ electrolysis.

**TABLE 1** | Key performance metrics for Ni(ref) and Ni–M (M = Fe, Co, Cu) electrodes. The TPB factor was calculated by normalizing the TPB length to that of Ni(ref) electrode. Apparent activation energies (App. $E_a$) were measured under $CO_2$/CO (80:20) atmosphere. Carbon-coverage quantified after exposure to $CO_2$/CO (40:60) at 650°C for 5 h (Figure 5J).

| | 5Fe95Ni | 5Co95Ni | Ni(ref) | 5Cu95Ni |
|---|---|---|---|---|
| TPB factor | 0.55 | 0.45 | 1 | 0.84 |
| App. $E_a$ (kJ $mol^{-1}$) | 91.6 | 68.8 | 111.9 | 99.9 |
| C Coverage (%) | 2.5 | 7.9 | 4.5 | 1.2 |

## 4 | Experimental Section

### 4.1 | Electrode Fabrication by Pulsed Laser Deposition

Symmetrical cells were fabricated using 8 mol% yttria-stabilized zirconia (YSZ, Nishimura) discs in the size of 4 mm radius and 3 mm thickness as the electrolyte substrate. For the electrochemical stability test, a 3YSZ (Kerafol) substrate of 80 μm thickness was used. Electrodes were prepared using a pulsed laser deposition (PLD) process to ensure uniform electrode structure among the different electrode samples. For the reference Ni/YSZ composite cermet electrode, a target for PLD was prepared by sintering a homogeneous mixture of NiO (Mechema) and YSZ (Tosoh) powders in a weight ratio of 56:44 (NiO:8YSZ) at 1400°C for 5 h. To fabricate the Ni–M/YSZ (M: Cu, Co, Fe) electrodes, different PLD targets were prepared by adding metal oxide powders (CuO, $Co_3O_4$, $Fe_2O_3$, purity > 99.99% trace metal basis, Sigma-Aldrich) to the NiO/YSZ mixture. In these targets, the molar percentage of the additional metal relative to the total transition metal was fixed at 5%, while the metal-to-YSZ ratio was maintained constant. The alloying concentration was fixed at 5 at% to minimize structural modifications of the Ni/YSZ cermet and to promote homogeneous alloy formation. Higher alloying levels have been reported to induce phase separation or substantial structural modifications in Ni-based alloy systems [118–123].

The PLD process was conducted at 700°C in an oxygen atmosphere at 50 mTorr for 3 h on both sides of the YSZ pellet. Following deposition, the samples were annealed at 1200°C for 1 h to prevent the agglomeration of Ni during the reduction process, which is essential for achieving the desired microstructure and ensuring proper electrode performance [124].

The Powder used for DRIFT analysis was synthesized by the glycine nitrate process, a combustion-based synthesis method. Nitrate precursors ($Ni(NO_3)_2 \cdot 6H_2O$, $Co(NO_3)_2 \cdot 6H_2O$, $Cu(NO_3)_2 \cdot 3H_2O$, $Fe(NO_3)_3 \cdot 9H_2O$, purity >98%, Sigma-Aldrich) of each metal and glycine were dissolved in water with the desired stoichiometry of the final compound and with a glycine-to-nitrate ratio of 0.55. The solution was stirred thoroughly to ensure solution homogeneity and was then heated on a hot plate to evaporate the water and obtain a powder after the combustion. The powders were calcined in air at 800°C to remove residual ash. After calcination, the powders were reduced at 650°C for 5 h in a 4% $H_2$/Ar atmosphere to produce the final Ni–M alloy powders.

### 4.2 | Characterization

The phase purity of each electrode was verified using X-ray diffraction (XRD) analysis, with Rietveld refinement performed through HighScore Plus software to quantify the phase composition and obtain the lattice parameter. Transmission electron microscopy (TEM; Talos F200X, Thermo Fisher Scientific) was conducted with samples prepared using a focused ion beam (FIB; NX5000m Hitachi High-Tech). Carbon deposition morphologies were examined using a scanning electron microscope (SEM; Inspect F50, FEI) and an optical microscope (LV150, Nikon). Raman spectroscopy (In Via Raman Microscope, Renishaw) was employed to analyze the properties of carbon formed on the electrodes under controlled carbon deposition conditions. Diffuse reflectance infrared Fourier transform spectroscopy (DRIFT) was conducted with an FT-IR spectrometer (Nicolet 6700, Thermo Fisher Scientific) along with a designated chamber (DiffuseIR, Pike Technologies) to investigate the surface intermediate species present on the samples at atmospheric pressure within a reactant gas environment. X-ray absorption spectroscopy (XAS) was conducted using the 1D beamline of the Pohang Light Source (PLS-2) for X-ray Absorption Near Edge structure (XANES) and Extended X-ray Absorption Fine Structure (EXAFS) analysis. The Co, Fe K-edge spectra were obtained in fluorescence mode. A reference Metal foil was measured independently without the sample, since the measured samples were thin-film deposited on a thick substrate. The XAS data were processed and fitted with the ATHENA and ARTEMIS software programs. Coordination number was obtained by fixing the $S_0^2$ value, which was obtained from the reference foils.

### 4.3 | Electrochemical Measurement

The symmetrical cell evaluation system was used for electrochemical measurements conducted in the temperature range of 650°C to 800°C under various $CO/CO_2$ conditions, controlled by the composition of the $CO/CO_2$ mixture. Impedance and performance measurements were performed using a Solartron 1260 frequency response analyzer and a 1287 A potentiostat/galvanostat electrochemical interface (Solartron Analytical). Impedance data were recorded at the open-circuit voltage (OCV) across a frequency range of 0.1 MHz to 0.1 Hz, with an AC perturbation of 1 mA to ensure a consistent electrochemical reaction at the electrodes. Galvanodynamic performance test was conducted by increasing the current at a rate of 1 mA/s starting from OCV. EIS fitting analysis was carried out using Z-View software for accurate data interpretation and modeling.

### 4.4 | Computational Details

Spin-polarized DFT calculations were performed (NFEC-2025-02-303332) using Vienna ab initio simulation package (VASP) [125]. The exchange-correlation energies were evaluated using the Perdew-Burke-Ernzerhof (PBE) functional based on generalized gradient approximation (GGA) [126]. The conjugate gradient (CG) method was adopted to optimize the simulation model, ensuring that the forces were below 0.03 eV and the energies were less than $10^{-4}$ eV. The plane-wave basis set employed an energy cutoff of 450 eV. The Methfessel-Paxton smearing method was adopted for all calculations. To account for Van der Waals (VdW) interaction, the DFT-D3 method with Becke-Johnson damping function was used [127]. The optimized lattice parameter of Ni was 3.48 Å. Then, we constructed a $(4 \times 4)$ supercell of the Ni(111) surface based on our experimental XRD data, and substituted one surface Ni atom with a dopant element to consider the doping ratio of 6.25% to model the experimental doping ratio of 5% considering the computational cost for simulating the larger size of supercells, which can describe the surface doping ratio of ≈5%. For all slab model

calculations, the bottom two layers were fixed as their bulk structure. To prevent the self-interaction between periodic slabs, the vacuum layer of 15 Å along the *c*-axis was employed. All calculations for the periodic slab model were applied $3 \times 3 \times 1$ Monkhorst-Pack k-points mesh grid [128]. The activation energies were calculated using the climbing image nudged-elastic band (Cl-NEB) method [129].

The adsorption energy ($E_{ad}$) was calculated as follows:

$$E_{ad} = E_{sys} - E_{clean} - E_{mol}$$

where $E_{ad}$ represents the adsorption energy, $E_{sys}$ represents the total energy of the system with adsorbates adsorbed on the surface, $E_{clean}$ represents the total energy of a clean surface, and $E_{mol}$ represents the total energy of an isolated adsorbate molecule.


## Acknowledgments

This study was financially supported by the Korea Institute of Energy Technology Evaluation and Planning (KETEP) (Nos. 20213030030040 and 20223030030090) and by the Institutional Research Program (No. 2E33912) of the Korea Institute of Science and Technology (KIST). Experiments at PLS-II were supported in part by MSIT and POSTECH.


## Conflicts of Interest

The authors declare no conflicts of interest.

## References


1. Q. Zhu, "Developments on $CO_2$-Utilization Technologies," *Clean Energy* 3, no. 2 (2019): 85–100.

2. S. Nitopi, E. Bertheussen, S. B. Scott, et al., "Progress and Perspectives of Electrochemical $CO_2$ Reduction on Copper in Aqueous Electrolyte," *Chemical Reviews* 119, no. 12 (2019): 7610–7672.

3. A. Hauch, R. Küngas, P. Blennow, et al., "Recent Advances in Solid Oxide Cell Technology for Electrolysis," *Science* 370, no. 6513 (2020): eaba6118.

4. L. Wang, Y. Zhang, M. Pérez-Fortes, et al., "Reversible Solid-Oxide Cell Stack Based Power-To-X-To-Power Systems: Comparison of Thermodynamic Performance," *Applied Energy* 275 (2020): 115330.

5. R. Küngas, "Review—Electrochemical $CO_2$ Reduction for CO Production: Comparison of Low- and High-Temperature Electrolysis Technologies," *Journal of the Electrochemical Society* 167, no. 4 (2020): 044508.

6. K. Ghaib and F.-Z. Ben-Fares, "Power-To-Methane: A State-Of-The-Art Review," *Renewable and Sustainable Energy Reviews* 81 (2018): 433–446.

7. M. S. Khan, Z. Lin, L. Lin, M. Abid, H. M. Ali, and C. Chen, "Techno-Economic Analysis of Solar-Driven Co-Electrolysis for Renewable Methanol Production Using Soec," *Energy Conversion and Management* 302 (2024): 118129.

8. S. Ali, K. Sørensen, and M. P. Nielsen, "Modeling a Novel Combined Solid Oxide Electrolysis Cell (SOEC)-Biomass Gasification Renewable Methanol Production System," *Renewable Energy* 154 (2020): 1025–1034.

9. R. G. Grim, D. Ravikumar, E. C. Tan, et al., "Electrifying the Production of Sustainable Aviation Fuel: The Risks, Economics, and Environmental Benefits of Emerging Pathways Including $CO_2$," *Energy & Environmental Science* 15, no. 11 (2022): 4798–4812.

10. Y. Zhou, S. Searle, and N. Pavlenko, "Current and Future Cost of e-Kerosene in the United States and Europe. I: International Council on Clean," Transportation Working Paper. (2022),14.

11. R. J. Detz, C. J. Ferchaud, A. J. Kalkman, et al., "Electrochemical $CO_2$ Conversion Technologies: State-Of-The-Art and Future Perspectives," *Sustainable Energy & Fuels* 7, no. 23 (2023): 5445–5472.

12. C. P. O'Brien, R. K. Miao, A. Shayesteh Zeraati, G. Lee, E. H. Sargent, and D. Sinton, "$CO_2$ Electrolyzers," *Chemical Reviews* 124, no. 7 (2024): 3648–3693.

13. P. Su-Ungkavatin, L. Tiruta-Barna, and L. Hamelin, "Biofuels, Electrofuels, Electric or Hydrogen?: A Review of Current and Emerging Sustainable Aviation Systems," *Progress in Energy and Combustion Science* 96 (2023): 101073.

14. T. L. Skafte, P. Blennow, J. Hjelm, and C. Graves, "Carbon Deposition and Sulfur Poisoning During $CO_2$ Electrolysis in Nickel-Based Solid Oxide Cell Electrodes," *Journal of Power Sources* 373 (2018): 54–60.

15. A. K. Clausen, M. Traulsen, P. V. Hendriksen, X. Sun, and A. Hauch, "CGO-Infiltrated Ni/YSZ SOEC Fuel Electrodes for Increased Carbon Tolerance During $CO_2$ Electrolysis," *ECS Transactions* 103, no. 1 (2021): 1945–1954.

16. H. Wang, F. Jiang, X. Wang, L. Ye, and K. Xie, "Enhanced $CO_2$ Electrolysis With the Modification of Ni–YSZ Cathodes by SDC in Microtubular Solid Oxide Electrolysis Cells," *Energy & Fuels* 36, no. 21 (2022): 13195–13202.

17. S. A. Barnett, B.-K. Park, and R. Scipioni, "Effect of Infiltration on Performance of Ni-YSZ Fuel Electrodes," *ECS Transactions* 91, no. 1 (2019): 1791–1797.

18. B.-K. Park, R. Scipioni, D. Cox, and S. A. Barnett, "Enhancement of Ni–$(Y_2O_3)_{0.08}(ZrO_2)_{0.92}$ Fuel Electrode Performance by Infiltration of $Ce_{0.8}Gd_{0.2}O_{2-\delta}$ Nanoparticles," *Journal of Materials Chemistry A* 8, no. 7 (2020): 4099–4106.

19. P. J. Gasper, Y. Lu, A. Y. Nikiforov, S. N. Basu, S. Gopalan, and U. B. Pal, "Detailed Electrochemical Performance and Microstructural Characterization of Nickel–Yttria Stabilized Zirconia Cermet Anodes Infiltrated With Nickel, Gadolinium Doped Ceria, and Nickel–Gadolinium Doped Ceria Nanoparticles," *Journal of Power Sources* 447 (2020): 227357.

20. S.-W. Kim, M. Park, H. Kim, et al., "Catalytic Effect of Pd-Ni Bimetallic Catalysts on High-Temperature Co-Electrolysis of Steam/$CO_2$ Mixtures," *Journal of the Electrochemical Society* 163, no. 11 (2016): F3171–F3178.

21. P. Błaszczak, M. Zając, A. Ducka, et al., "High-Temperature Co-Electrolysis of $CO_2/H_2O$ and Direct Methanation Over Co-Impregnated SOEC. Bimetallic Synergy Between Co and Ni," *International Journal of Hydrogen Energy* 47, no. 82 (2022): 35017–35037.

22. H. Y. Jeong, S. W. Kim, Y. Bae, K. J. Yoon, J. H. Lee, and J. Hong, "Effect of Fe Infiltration to Ni/YSZ Solid-Oxide-Cell Fuel Electrode on Steam/$CO_2$ Co-Electrolysis," *International Journal of Energy Research* 43, no. 9 (2019): 4949–4958.

23. C. M. Grgicak, M. M. Pakulska, J. S. O'Brien, and J. B. Giorgi, "Synergistic Effects of $Ni_{1-x}Co_x$-YSZ and $Ni_{1-x}Cu_x$-YSZ Alloyed Cermet SOFC Anodes for Oxidation of Hydrogen and Methane Fuels Containing $H_2S$," *Journal of Power Sources* 183, no. 1 (2008): 26–33.

24. D. Chen, J. Zhang, M. Barreau, et al., "Ni-Doped $CeO_2$ Nanoparticles to Promote and Restore the Performance of Ni/YSZ Cathodes for $CO_2$ Electroreduction," *Applied Surface Science* 611 (2023): 155767.

25. M. Zheng, S. Wang, Y. Yang, and C. Xia, "Barium Carbonate as a Synergistic Catalyst for the $H_2O/CO_2$ Reduction Reaction at Ni–Yttria

Stabilized Zirconia Cathodes for Solid Oxide Electrolysis Cells," *Journal of Materials Chemistry A* 6, no. 6 (2018): 2721–2729.

26. Y. Song, Z. Zhou, X. Zhang, et al., "Pure $CO_2$ Electrolysis Over an Ni/YSZ Cathode in a Solid Oxide Electrolysis Cell," *Journal of Materials Chemistry A* 6, no. 28 (2018): 13661–13667.

27. Y. Chen, J. Bunch, C. Jin, C. Yang, and F. Chen, "Performance Enhancement of Ni-YSZ Electrode by Impregnation of $Mo_{0.1}Ce_{0.9}O_{2+\delta}$," *Journal of Power Sources* 204 (2012): 40–45.

28. S. Liu, Q. Liu, and J.-L. Luo, "$CO_2$-to-Co Conversion on Layered Perovskite With In Situ Exsolved Co–Fe Alloy Nanoparticles: An Active and Stable Cathode for Solid Oxide Electrolysis Cells," *Journal of Materials Chemistry A* 4, no. 44 (2016): 17521–17528.

29. S. W. Lee, T. H. Nam, M. Kim, et al., "Enhancing $CO_2$ Electrolysis Performance With Various Metal Additives (Co, Fe, Ni, and Ru)–Decorating the $La(Sr)Fe(Mn)O_3$ Cathode In Solid Oxide Electrolysis Cells," *Inorganic Chemistry Frontiers* 10, no. 12 (2023): 3536–3543.

30. M. Li, J. Hou, Y. Fan, X. Xi, X.-Z. Fu, and J.-L. Luo, "Interface Modification of Ru-$CeO_2$ Co-Infiltrated SFM Electrode and Construction of SDC/YSZ Bilayer Electrolyte for Direct $CO_2$ Electrolysis," *Electrochimica Acta* 426 (2022): 140771.

31. W. Wang, H. Li, C. Y. Regalado Vera, et al., "Improving the Performance for Direct Electrolysis of $CO_2$ in Solid Oxide Electrolysis Cells With a $Sr_{1.9}Fe_{1.5}Mo_{0.5}O_{6-\delta}$ Electrode via Infiltration of $Pr_6O_{11}$ Nanoparticles," *Journal of Materials Chemistry A* 11, no. 16 (2023): 9039–9048.

32. J. K. Nørskov, F. Studt, F. Abild-Pedersen, and T. Bligaard, *Fundamental Concepts in Heterogeneous Catalysis* (John Wiley & Sons, 2014).

33. A. Logadottir, T. H. Rod, J. K. Nørskov, B. Hammer, S. Dahl, and C. J. H. Jacobsen, "The Brønsted–Evans–Polanyi Relation and the Volcano Plot for Ammonia Synthesis Over Transition Metal Catalysts," *Journal of Catalysis* 197, no. 2 (2001): 229–231.

34. I. E. L. Stephens, A. S. Bondarenko, F. J. Perez-Alonso, et al., "Tuning the Activity of Pt (111) for Oxygen Electroreduction by Subsurface Alloying," *Journal of the American Chemical Society* 133, no. 14 (2011): 5485–5491.

35. M. Escudero-Escribano, P. Malacrida, M. H. Hansen, et al., "Tuning the Activity of Pt Alloy Electrocatalysts by Means of the Lanthanide Contraction," *Science* 352, no. 6281 (2016): 73–76.

36. F. Calle-Vallejo, J. Tymoczko, V. Colic, et al., "Finding Optimal Surface Sites on Heterogeneous Catalysts by Counting Nearest Neighbors," *Science* 350, no. 6257 (2015): 185–189.

37. B. Hammer and J. K. Norskov, "Why Gold Is the Noblest of All the Metals," *Nature* 376, no. 6537 (1995): 238–240.

38. J. Greeley and J. K. Nørskov, "A General Scheme for the Estimation of Oxygen Binding Energies on Binary Transition Metal Surface Alloys," *Surface Science* 592, no. 1–3 (2005): 104–111.

39. T. Adit Maark and B. R. K. Nanda, "Enhancing $CO_2$ Electroreduction by Tailoring Strain and Ligand Effects in Bimetallic Copper–Rhodium and Copper–Nickel Heterostructures," *Journal of Physical Chemistry C* 121, no. 8 (2017): 4496–4504.

40. H. Thirumalai and J. R. Kitchin, "Investigating the Reactivity of Single Atom Alloys Using Density Functional Theory," *Topics in Catalysis* 61 (2018): 462–474.

41. A. Cho, J. Ko, B.-K. Kim, and J. W. Han, "Electrocatalysts With Increased Activity for Coelectrolysis of Steam and Carbon Dioxide in Solid Oxide Electrolyzer Cells," *ACS Catalysis* 9, no. 2 (2018): 967–976.

42. X.-K. Gu, J. S. Carneiro, and E. Nikolla, "First-Principles Study of High Temperature $CO_2$ Electrolysis on Transition Metal Electrocatalysts," *Industrial & Engineering Chemistry Research* 56, no. 21 (2017): 6155–6163.

43. C. Liu, T. R. Cundari, and A. K. Wilson, "$CO_2$ Reduction on Transition Metal (Fe, Co, Ni, and Cu) Surfaces: In Comparison With Homogeneous Catalysis," *Journal of Physical Chemistry C* 116, no. 9 (2012): 5681–5688.

44. J. Carneiro, X.-K. Gu, E. Tezel, and E. Nikolla, "Electrochemical Reduction of $CO_2$ on Metal-Based Cathode Electrocatalysts of Solid Oxide Electrolysis Cells," *Industrial & Engineering Chemistry Research* 59, no. 36 (2020): 15884–15893.

45. X. Gao, L. Ye, and K. Xie, "In-Situ Exsolved Ni-Cu Alloy Nanoparticles for Optimization of Perovskite Electrodes in Solid Oxide Electrolysis Cell," *Fuel* 371 (2024): 131959.

46. W. Cui, X. Yang, M. Ma, et al., "Boosting Catalytic and $CO_2$ Adsorption Ability by In Situ Cu Nanoparticle Exsolution for Solid Oxide Electrolysis Cell Cathode," *Ceramics International* 49, no. 16 (2023): 27214–27221.

47. W. An, D. Gatewood, B. Dunlap, and C. H. Turner, "Catalytic Activity of Bimetallic Nickel Alloys for Solid-Oxide Fuel Cell Anode Reactions From Density-Functional Theory," *Journal of Power Sources* 196, no. 10 (2011): 4724–4728.

48. S. Kim, C. Kim, J. H. Lee, J. Shin, T.-H. Lim, and G. Kim, "Tailoring Ni-Based Catalyst by Alloying With Transition Metals (M= Ni, Co, Cu, and Fe) for Direct Hydrocarbon Utilization of Energy Conversion Devices," *Electrochimica Acta* 225 (2017): 399–406.

49. N. Galea, D. Knapp, and T. Ziegler, "Density Functional Theory Studies of Methane Dissociation on Anode Catalysts in Solid-Oxide Fuel Cells: Suggestions for Coke Reduction," *Journal of Catalysis* 247, no. 1 (2007): 20–33.

50. L. Zhu and A. E. DePristo, "Microstructures of Bimetallic Clusters: Bond Order Metal Simulator for Disordered Alloys," *Journal of Catalysis* 167, no. 2 (1997): 400–407.

51. A. A. Peterson, F. Abild-Pedersen, F. Studt, J. Rossmeisl, and J. K. Nørskov, "How Copper Catalyzes the Electroreduction of Carbon Dioxide Into Hydrocarbon Fuels," *Energy & Environmental Science* 3, no. 9 (2010): 1311–1315.

52. J. Horlyck, C. Lawrey, E. C. Lovell, R. Amal, and J. Scott, "Elucidating the Impact of Ni and Co Loading on the Selectivity of Bimetallic NiCo Catalysts for Dry Reforming of Methane," *Chemical Engineering Journal* 352 (2018): 572–580.

53. E. Ruckenstein and H. Y. Wang, "Carbon Deposition and Catalytic Deactivation During $CO_2$ Reforming of $CH_4$ Over Co/$\gamma$-$Al_2O_3$ Catalysts," *Journal of Catalysis* 205, no. 2 (2002): 289–293.

54. J. Estephane, S. Aouad, S. Hany, et al., "$CO_2$ Reforming of Methane Over Ni–Co/ZSM5 Catalysts. Aging and Carbon Deposition Study," *International Journal of Hydrogen Energy* 40, no. 30 (2015): 9201–9208.

55. S. A. Theofanidis, V. V. Galvita, H. Poelman, and G. B. Marin, "Enhanced Carbon-Resistant Dry Reforming Fe-Ni Catalyst: Role of Fe," *ACS Catalysis* 5, no. 5 (2015): 3028–3039.

56. E. Pippel, J. Woltersdorf, and H. J. Grabke, "Microprocesses of Metal Dusting on Iron-Nickel Alloys and Their Dependence on the Alloy Composition," *Materials and Corrosion* 54, no. 10 (2003): 747–751.

57. M. Shahid, C. He, S. Sankarasubramanian, V. K. Ramani, and S. Basu, "$Co_3O_4$-Impregnated NiO–YSZ: An Efficient Catalyst for Direct Methane Electrooxidation," *ACS Applied Materials & Interfaces* 12, no. 29 (2020): 32578–32590.

58. O. Costa-Nunes, R. J. Gorte, and J. M. Vohs, "Comparison of the Performance of Cu–$CeO_2$–YSZ and Ni–YSZ Composite SOFC Anodes With $H_2$, CO, and Syngas," *Journal of Power Sources* 141, no. 2 (2005): 241–249.

59. E. W. Park, H. Moon, M. Park, and S. H. Hyun, "Fabrication and Characterization of Cu–Ni–YSZ SOFC Anodes for Direct Use of Methane via Cu-Electroplating," *International Journal of Hydrogen Energy* 34, no. 13 (2009): 5537–5545.

60. S. Liu, Q. Liu, and J.-L. Luo, "Highly Stable and Efficient Catalyst With In Situ Exsolved Fe–Ni Alloy Nanospheres Socketed on an Oxygen Deficient Perovskite for Direct $CO_2$ Electrolysis," *ACS Catalysis* 6, no. 9 (2016): 6219–6228.

61. P. J. Schilling, J. H. He, R. C. Tittsworth, and E. Ma, "Two-Phase Coexistence Region in Mechanically Alloyed Cu–Fe: An X-Ray Absorption Near-Edge Structure Study," *Acta Materialia* 47, no. 8 (1999): 2525–2537.

62. D. J. Sprouster and M. C. Ridgway, "Ion Beam Formation and Modification of Cobalt Nanoparticles," *Applied Sciences* 2, no. 2 (2012): 396–442.

63. J. L. Alfke, A. Müller, A. H. Clark, et al., "BCC-Cu Nanoparticles: From a Transient to a Stable Allotrope by Tuning Size and Reaction Conditions," *Physical Chemistry Chemical Physics* 24, no. 39 (2022): 24429–24438.

64. S. Olvera, J. Sánchez-Marcos, F. J. Palomares, E. Salas, E. M. Arce, and P. Herrasti, "Characterization and Corrosion Behaviour of CoNi Alloys Obtained by Mechanical Alloying," *Materials Characterization* 93 (2014): 79–86.

65. H. Wu, H. Liu, W. Yang, and D. He, "Synergetic Effect of Ni and Co in Ni–Co/SBA-15-Cd Catalysts and Their Catalytic Performance in Carbon Dioxide Reforming of Methane to Syngas," *Catalysis Science & Technology* 6, no. 14 (2016): 5631–5646.

66. X. Yao, Q. Cheng, Y. Attada, et al., "Atypical Stability of Exsolved Ni– Fe Alloy Nanoparticles on Double Layered Perovskite for $CO_2$ Dry Reforming of Methane," *Applied Catalysis, B: Environmental* 328 (2023): 122479.

67. L. R. Winter, E. Gomez, B. Yan, S. Yao, and J. G. Chen, "Tuning Ni-Catalyzed $CO_2$ Hydrogenation Selectivity via Ni-Ceria Support Interactions and Ni– Fe Bimetallic Formation," *Applied Catalysis, B: Environmental* 224 (2018): 442–450.

68. A. J. Flegler, T. E. Burye, Q. Yang, and J. D. Nicholas, "Cubic Yttria Stabilized Zirconia Sintering Additive Impacts: A Comparative Study," *Ceramics International* 40, no. 10 (2014): 16323–16335.

69. A. Hauch and A. Georg, "Diffusion in the Electrolyte and Charge-Transfer Reaction at the Platinum Electrode in Dye-Sensitized Solar Cells," *Electrochimica Acta* 46, no. 22 (2001): 3457–3466.

70. T. Kawashima, S. Miyoshi, Y. Shibuta, and S. Yamaguchi, "Particle Size Dependence of Polarization of Ni/YSZ Cermet Anodes for Solid Oxide Fuel Cells," *Journal of Power Sources* 234 (2013): 147–153.

71. T. Abe, H. Fukuda, Y. Iriyama, and Z. Ogumi, "Solvated Li-Ion Transfer at Interface Between Graphite and Electrolyte," *Journal of the Electrochemical Society* 151, no. 8 (2004): A1120.

72. H. Lv, L. Lin, X. Zhang, et al., "In Situ Investigation of Reversible Exsolution/Dissolution of CoFe Alloy Nanoparticles in a Co-Doped $Sr_2Fe_{1.5}Mo_{0.5}O_{6-\delta}$ Cathode for $CO_2$ Electrolysis," *Advanced Materials* 32, no. 6 (2020): 1906193.

73. H. Seo, S. Jang, W. Lee, et al., "Highly Efficient, Coke-Free Electrolysis of Dry $CO_2$ in Solid Oxide Electrolysis Cells," *Chemical Engineering Journal* 481 (2024): 148532.

74. P. Caliandro, A. Nakajo, S. Diethelm, and J. Van herle, "Model-Assisted Identification of Solid Oxide Cell Elementary Processes by Electrochemical Impedance Spectroscopy Measurements," *Journal of Power Sources* 436 (2019): 226838.

75. Q. Jiang, Z. Chen, J. Tong, M. Yang, Z. Jiang, and C. Li, "Direct Thermolysis of $CO_2$ Into CO and $O_2$," *Chemical Communications* 53, no. 6 (2017): 1188–1191.

76. J. Liang and M. Han, "Different Performance and Mechanisms of $CO_2$ Electrolysis With CO and $H_2$ as Protective Gases in Solid Oxide Electrolysis Cell," *International Journal of Hydrogen Energy* 47, no. 43 (2022): 18606–18618.

77. J. Hong, A. Bhardwaj, H. Bae, I. Kim, and S.-J. Song, "Electrochemical Impedance Analysis of SOFC With Transmission Line Model Using Distribution of Relaxation Times (DRT)," *Journal of the Electrochemical Society* 167, no. 11 (2020): 114504.

78. H. Sumi, H. Shimada, Y. Yamaguchi, T. Yamaguchi, and Y. Fujishiro, "Degradation Evaluation by Distribution of Relaxation Times Analysis for Microtubular Solid Oxide Fuel Cells," *Electrochimica Acta* 339 (2020): 135913.

79. S. Singhal, *High Temperature SolidOxide Fuel Cells: Fundamentals, Design and Applications* (Elsevier, 2003).

80. L. Lu, W. Liu, J. Wang, et al., "Long-Term Stability of Carbon Dioxide Electrolysis in a Large-Scale Flat-Tube Solid Oxide Electrolysis Cell Based on Double-Sided Air Electrodes," *Applied Energy* 259 (2020): 114130.

81. B. Zhang, S. Zhang, Z. Zhang, K. Tang, and C. Xia, "Metal-Supported Solid Oxide Electrolysis Cell for Direct $CO_2$ Electrolysis Using Stainless Steel Based Cathode," *Journal of Power Sources* 556 (2023): 232467.

82. Y. Nishiyama, K. Moriguchi, N. Otsuka, and T. Kudo, "Improving Metal Dusting Resistance of Transition-Metals and Ni-Cu Alloys," *Materials and Corrosion* 56, no. 11 (2005): 806–813.

83. G. Ertl, H. Knözinger, and J. Weitkamp, *Handbook of Heterogeneous Catalysis* (VCH Weinheim, 1997), 2.

84. P. I. Zámostný and J. W. Chorkendorff, "Niemantsverdriet: Concepts of Modern Catalysis and Kinetics," *Chemické listy* 98, no. 5 (2004): 268.

85. J. Cai, Y. Han, S. Chen, et al., "$CO_2$ Activation on Ni (111) and Ni (100) Surfaces in the Presence of $H_2O$: An Ambient-Pressure X-Ray Photoelectron Spectroscopy Study," *Journal of Physical Chemistry C* 123, no. 19 (2019): 12176–12182.

86. S. E. Collins, M. A. Baltanás, and A. L. Bonivardi, "Infrared Spectroscopic Study of the Carbon Dioxide Adsorption on the Surface of $Ga_2O_3$ Polymorphs," *Journal of Physical Chemistry B* 110, no. 11 (2006): 5498–5507.

87. A. Solis-Garcia, J. F. Louvier-Hernandez, A. Almendarez-Camarillo, and J. C. Fierro-Gonzalez, "Participation of Surface Bicarbonate, Formate and Methoxy Species in the Carbon Dioxide Methanation Catalyzed by $ZrO_2$-Supported Ni," *Applied Catalysis, B: Environmental* 218 (2017): 611–620.

88. H. L. Huynh, J. Zhu, G. Zhang, et al., "Promoting Effect of Fe on Supported Ni Catalysts in $CO_2$ Methanation by In Situ Drifts and DFT Study," *Journal of Catalysis* 392 (2020): 266–277.

89. H.-J. Freund and R. P. Messmer, "On the Bonding and Reactivity of $CO_2$ on Metal Surfaces," *Surface Science* 172, no. 1 (1986): 1–30.

90. D. Shen, M. Huo, L. Li, et al., "Effects of Alumina Morphology on Dry Reforming of Methane over $Ni/Al_2O_3$ Catalysts," *Catalysis Science & Technology* 10, no. 2 (2020): 510–516.

91. O. Pozdnyakova, D. Teschner, A. Wootsch, et al., "Preferential CO Oxidation in Hydrogen (PROX) on Ceria-Supported Catalysts, Part I: Oxidation State and Surface Species on $Pt/CeO_2$ Under Reaction Conditions," *Journal of Catalysis* 237, no. 1 (2006): 1–16.

92. R. B. David, A. R. Head, S. Lin, A. B. Yaacov, M. A. Andres, and B. Eren, "Molecular-Level Insights into $CO_2$ Activation on Ni (111) From In Situ Infrared Spectroscopy," *Cell Reports Physical Science* 5, no. 4 (2024): 101890, https://doi.org/10.1016/j.xcrp.2024.101890.

93. N. Colthup, *Introduction to Infrared and Raman Spectroscopy* (Elsevier, 2012).

94. J. Mascetti and M. Tranquille, "Fourier Transform Infrared Studies of Atomic Titanium, Vanadium, Chromium, Iron, Cobalt, Nickel and Copper Reactions With Carbon Dioxide in Low-Temperature Matrices," *Journal of Physical Chemistry* 92, no. 8 (1988): 2177–2184.

95. E. Nikolla, J. Schwank, and S. Linic, "Promotion of the Long-Term Stability of Reforming Ni Catalysts by Surface Alloying," *Journal of Catalysis* 250, no. 1 (2007): 85–93.

96. I. Gavrielatos, V. Drakopoulos, and S. Neophytides, "Carbon Tolerant Ni–Au SOFC Electrodes Operating Under Internal Steam Reforming Conditions," *Journal of Catalysis* 259, no. 1 (2008): 75–84.

97. M. Boder and R. Dittmeyer, "Catalytic Modification of Conventional SOFC Anodes With a View to Reducing Their Activity for Direct Internal Reforming of Natural Gas," *Journal of Power Sources* 155, no. 1 (2006): 13–22.

98. T. Margossian, K. Larmier, S. M. Kim, F. Krumeich, C. Müller, and C. Copéret, "Supported Bimetallic NiFe Nanoparticles Through Colloid Synthesis for Improved Dry Reforming Performance," *ACS Catalysis* 7, no. 10 (2017): 6942–6948.

99. M. Koike, D. Li, Y. Nakagawa, and K. Tomishige, "A Highly Active and Coke-Resistant Steam Reforming Catalyst Comprising Uniform Nickel-Iron Alloy Nanoparticles," *Chemsuschem* 5, no. 12 (2012): 2312–2314.

100. S. M. Kim, P. M. Abdala, T. Margossian, et al., "Cooperativity and Dynamics Increase the Performance of NiFe Dry Reforming Catalysts," *Journal of the American Chemical Society* 139, no. 5 (2017): 1937–1949.

101. X. Gao, Z. Tan, K. Hidajat, and S. Kawi, "Highly Reactive Ni-Co/$SiO_2$ Bimetallic Catalyst via Complexation With Oleylamine/Oleic Acid Organic Pair for Dry Reforming of Methane," *Catalysis Today* 281 (2017): 250–258.

102. I. V. Zagaynov, "Active Components of Catalysts of Methane Conversion to Synthesis Gas: Brief Perspectives," *Energy & Fuels* 35, no. 11 (2021): 9124–9136.

103. D. L. Trimm, "The Formation and Removal of Coke From Nickel Catalyst," *Catalysis Reviews* 16, no. 1 (1977): 155–189.

104. H. Dai, A. G. Rinzler, P. Nikolaev, A. Thess, D. T. Colbert, and R. E. Smalley, "Single-Wall Nanotubes Produced by Metal-Catalyzed Disproportionation of Carbon Monoxide," *Chemical Physics Letters* 260, no. 3–4 (1996): 471–475.

105. K. Girona, J. Laurencin, J. Fouletier, and F. Lefebvre-Joud, "Carbon Deposition in $CH_4/CO_2$ Operated SOFC: Simulation and Experimentation Studies," *Journal of Power Sources* 210 (2012): 381–391.

106. A. Utz, A. Leonide, A. Weber, and E. Ivers-Tiffée, "Studying the CO–$CO_2$ Characteristics of SOFC Anodes by Means of Patterned Ni Anodes," *Journal of Power Sources* 196, no. 17 (2011): 7217–7224.

107. M. Torimoto and Y. Sekine, "Effects of Alloying for Steam or Dry Reforming of Methane: A Review of Recent Studies," *Catalysis Science & Technology* 12, no. 11 (2022): 3387–3411.

108. F. Besenbacher, I. Chorkendorff, B. S. Clausen, et al., "Design of a Surface Alloy Catalyst for Steam Reforming," *Science* 279, no. 5358 (1998): 1913–1915.

109. A. Chatla, M. M. Ghouri, O. W. El Hassan, N. Mohamed, A. V. Prakash, and N. O. Elbashir, "An Experimental and First Principles DFT Investigation on the Effect of Cu Addition to Ni/$Al_2O_3$ Catalyst for the Dry Reforming of Methane," *Applied Catalysis, A: General* 602 (2020): 117699.

110. B. Li, W. Gao, and Q. Jiang, "Electronic and Geometric Determinants of Adsorption: Fundamentals and Applications," *Journal of Physics: Energy* 3, no. 2 (2021): 022001.

111. S. McIntosh and R. J. Gorte, "Direct Hydrocarbon Solid Oxide Fuel Cells," *Chemical Reviews* 104, no. 10 (2004): 4845–4866.

112. J. Sinfelt, "Catalytic Hydrogenolysis and Dehydrogenation Over Copper-Nickel Alloys," *Journal of Catalysis* 24, no. 2 (1972): 283–296.

113. M. T. Tavares, I. Alstrup, and C. A. A. Bernardo, "Coking and Decoking During Methanation and Methane Decomposition on Ni-Cu Supported Catalysts," *Materials and Corrosion* 50, no. 12 (1999): 681–685.

114. H. Kim, C. Lu, W. L. Worrell, J. M. Vohs, and R. J. Gorte, "Cu-Ni Cermet Anodes for Direct Oxidation of Methane in Solid-Oxide Fuel Cells," *Journal of the Electrochemical Society* 149, no. 3 (2002): A247.

115. S.-I. Lee, J. M. Vohs, and R. J. Gorte, "A Study of SOFC Anodes Based on Cu-Ni and Cu-Co Bimetallics in $CeO_2$-YSZ," *Journal of the Electrochemical Society* 151, no. 9 (2004): A1319.

116. J. H. Park, S. Oh, B. C. Yang, et al., "Pushing the Envelope of Physical Vapor Deposited Thin-Film Based Solid Oxide Fuel Cells for 500°C Operation: Securing 1 W $cm^{-2}$ Performance, 1000 h Stability, Scale Up to 15 W Power, and Associated Limitations," *Chemical Engineering Journal* 515 (2025): 163441.

117. W. Lee, M. Lang, R. Costa, I.-S. Lee, Y.-S. Lee, and J. Hong, "Enhancing Uniformity and Performance in Solid Oxide Fuel Cells With Double Symmetry Interconnect Design," *Applied Energy* 381 (2025): 125178.

118. I. Ohnuma, S. Shimenouchi, T. Omori, K. Ishida, and R. Kainuma, "Experimental Determination and Thermodynamic Evaluation of Low-Temperature Phase Equilibria in the Fe–Ni Binary System," *Calphad* 67 (2019): 101677.

119. T. O. Menteş, N. Stojić, E. Vescovo, J. M. Ablett, M. A. Niño, and A. Locatelli, "Vacancy-Mediated Fcc/Bcc Phase Separation in $Fe_{1-x}Ni_x$ Ultrathin Films," *Physical Review B* 94, no. 8 (2016): 085402.

120. M. Miyake, S. Matsumoto, M. Iwami, S. Nishimoto, and Y. Kameshima, "Electrochemical Performances of $Ni_{1-x}Cu_x$/SDC Cermet Anodes for Intermediate-Temperature SOFCs Using Syngas Fuel," *International Journal of Hydrogen Energy* 41, no. 31 (2016): 13625–13631.

121. H. Kan and H. Lee, "Enhanced Stability of Ni-Fe/GDC Solid Oxide Fuel Cell Anodes for Dry Methane Fuel," *Catalysis Communications* 12, no. 1 (2010): 36–39.

122. Y. Ishibashi, K. Matsumoto, S. Futamura, et al., "Improved Redox Cycling Durability in Alternative Ni Alloy-Based SOFC Anodes," *Journal of the Electrochemical Society* 167, no. 12 (2020): 124517.

123. M. Kateb, J. T. Gudmundsson, and S. Ingvarsson, "Effect of Atomic Ordering on the Magnetic Anisotropy of Single Crystal $Ni_{80}Fe_{20}$," *AIP Advances* 9, no. 3 (2019): 035308, https://doi.org/10.1063/1.5088602.

124. H.-S. Noh, J.-W. Son, H. Lee, H.-I. Ji, J.-H. Lee, and H.-W. Lee, "Suppression of Ni Agglomeration in PLD Fabricated Ni-YSZ Composite for Surface Modification of SOFC Anode," *Journal of the European Ceramic Society* 30, no. 16 (2010): 3415–3423.

125. G. Kresse and J. Furthmüller, "Efficient Iterative Schemes for Ab Initio Total-Energy Calculations Using a Plane-Wave Basis Set," *Physical Review B* 54, no. 16 (1996): 11169–11186.

126. J. P. Perdew, K. Burke, and M. Ernzerhof, "Generalized Gradient Approximation Made Simple," *Physical Review Letters* 77, no. 18 (1996): 3865–3868.

127. S. Grimme, S. Ehrlich, and L. Goerigk, "Effect of the Damping Function in Dispersion Corrected Density Functional Theory," *Journal of Computational Chemistry* 32, no. 7 (2011): 1456–1465.

128. H. J. Monkhorst and J. D. Pack, "Special Points for Brillouin-Zone Integrations," *Physical Review B* 13, no. 12 (1976): 5188–5192.

129. G. Henkelman, B. P. Uberuaga, and H. Jónsson, "A Climbing Image Nudged Elastic Band Method for Finding Saddle Points and Minimum Energy Paths," *Journal of Chemical Physics* 113, no. 22 (2000): 9901–9904.

## Supporting Information

Additional supporting information can be found online in the Supporting Information section.

Table S1. Calculation of the TPB factor for each alloyed Ni/YSZ electrode based on mean particle sizes of Ni and YSZ phase, normalized to the Ni/YSZ reference electrode. Table S2. Structural parameters around Co and Fe atoms in 5Cu95Ni/YSZ and 5Fe95Ni/YSZ samples with corresponding reference foils extracted from EXAFS curve fitting. Table S3. Reaction energy and activation energy of $CO_2$ dissociation on Ni(111), Co-doped (111), Cu-doped (111), and Fe-doped (111). Table S4. Summary of key performance metrics for all samples at 650°C and 800°C, based on the data presented in Figure 3. Figure S1. A-D) BF-TEM images of prepared samples. E-H) Diffraction pattern obtained from the marked area of BF-TEM images. The lattice parameter derived from patterns involves an estimated error of ~0.005 nm due to pixel resolution in data processing. Figure S2. Particle size distributions and corresponding statistical parameters (mean, median, and standard deviation) for the prepared samples: (A) YSZ and (B) Ni-M. Figure S3. The normalized Ni K-edge XANES spectra of samples with reference to the Ni metal foil. Figure S4. Cross-sectional SEM images of the samples. Figure S5. SEM Images of samples at (A-D) 5 h exposed, (E-H) 10 h exposed, and (I-L) 15 h exposed. Figure S6. Optimized structure of clean surface, *$CO_2$, *CO, *O, *CO + *O, and *C on Ni(111), Co doped (111), Cu doped (111), and Fe doped (111). The value below each figure represents the adsorption energy. Figure S7. Top-view of the initial state (IS), transition state (TS), and final state (FS) for $CO_2$ dissociation reaction on Ni(111), Co doped (111), Cu doped (111), and Fe doped (111). Figure S8. CO adsorption energy with different doping ratios on Ni(111), Co doped (111), Cu doped (111), and Fe doped (111). Figure S9. In-situ DRIFT spectra of various samples measured in a $CO_2$ atmosphere at 30°C. (A) Gaseous CO, (B) gaseous $CO_2$, and (C) adsorbed $CO_2$ peak. Figure S10. Optical images of samples treated in $CO_2$/CO (40:60) at 650°C for 10 h. Figure S11. Raman analysis for samples exposed for 5, 10, and 15 hours. Figure S12. Images from the long-term stability test presented in Figure 8: (A) Digital photographs of the cathodic electrodes after the test; (B) SEM Images of the cathodic electrode showing carbon deposition after the test.